The Astrophysical Journal Supplement Series, 209:2 (15pp), 2013 November doi:10.1088/0067-0049/209/1/2
© 2013. The American Astronomical Society. All rights reserved. Printed in the U.S.A.

THE BOLOCAM GALACTIC PLANE SURVEY. X. A COMPLETE SPECTROSCOPIC CATALOG OF DENSE MOLECULAR GAS OBSERVED TOWARD 1.1 mm DUST CONTINUUM SOURCES WITH $7\overset{\circ}{.}5 \leqslant l \leqslant 194^{\circ}$

Yancy L. Shirley[1,2], Timothy P. Ellsworth-Bowers[3], Brian Svoboda[1], Wayne M. Schlingman[3], Adam Ginsburg[3], Erik Rosolowsky[4], Thomas Gerner[5], Steven Mairs[6], Cara Battersby[3], Guy Stringfellow[3], Miranda K. Dunham[7], Jason Glenn[3], and John Bally[3]
[1] Steward Observatory, 933 North Cherry Avenue, Tucson, AZ 85721, USA
[2] Adjunct Astronomer, The National Radio Astronomy Observatory
[3] CASA, University of Colorado, CB 389, Boulder, CO 80309, USA
[4] Department of Physics, University of Alberta, 4-181 CCIS Edmonton AB T6G 2E1, Canada
[5] Max-Planck-Institut für Astronomie (MPIA), Knigstuhl 17, D-69117 Heidelberg, Germany
[6] Department of Physics and Astronomy, University of Victoria, P.O. Box 3055, STN CSC, Victoria, BC V8W 3P6, Canada
[7] Department of Astronomy, Yale University, P.O. Box 208101, New Haven, CT 06520, USA
Received 2013 June 20; accepted 2013 August 18; published 2013 October 11

ABSTRACT

The Bolocam Galactic Plane Survey (BGPS) is a 1.1 mm continuum survey of dense clumps of dust throughout the Galaxy covering 170 deg^2. We present spectroscopic observations using the Heinrich Hertz Submillimeter Telescope of the dense gas tracers, HCO^+ and N_2H^+ 3–2, for all 6194 sources in the BGPS v1.0.1 catalog between $7\overset{\circ}{.}5 \leqslant l \leqslant 194^{\circ}$. This is the largest targeted spectroscopic survey of dense molecular gas in the Milky Way to date. We find unique velocities for 3126 (50.5%) of the BGPS v1.0.1 sources observed. Strong N_2H^+ 3–2 emission ($T_{mb} > 0.5$ K) without HCO^+ 3–2 emission does not occur in this catalog. We characterize the properties of the dense molecular gas emission toward the entire sample. HCO^+ is very sub-thermally populated and the 3–2 transitions are optically thick toward most BGPS clumps. The median observed line width is 3.3 km s^{-1} consistent with supersonic turbulence within BGPS clumps. We find strong correlations between dense molecular gas integrated intensities and 1.1 mm peak flux and the gas kinetic temperature derived from previously published NH_3 observations. These intensity correlations are driven by the sensitivity of the 3–2 transitions to excitation conditions rather than by variations in molecular column density or abundance. We identify a subset of 113 sources with stronger N_2H^+ than HCO^+ integrated intensity, but we find no correlations between the N_2H^+/HCO^+ ratio and 1.1 mm continuum flux density, gas kinetic temperature, or line width. Self-absorbed profiles are rare (1.3%).

Key words: Galaxy: kinematics and dynamics – ISM: clouds – ISM: structure – radio lines: ISM – stars: formation– surveys

Online-only material: color figures, machine-readable tables

1. INTRODUCTION

In the last few years, comprehensive surveys of the Milky Way galaxy have been performed at submillimeter and millimeter wavelengths that have imaged dust continuum emission and have provided the most complete census of embedded sites of star formation in our Galaxy. The Bolocam Galactic Plane Survey (BGPS) version 1.0 mapped over 170 deg^2 of the Galactic plane at 1.1 mm (Aguirre et al. 2011) and has cataloged over 8400 continuum sources (Rosolowsky et al. 2010). The BGPS observed the entire first quadrant in a strip that is 1° wide in galactic latitude with selected regions observed in the second ($l \approx 98^{\circ}$, 111°, 133°–136°), third ($188^{\circ} \leqslant l \leqslant 192^{\circ}$) and fourth quadrants ($l > 350^{\circ}$). A complementary survey at 870 μm, ATLASGAL, has mapped sections of the southern Milky Way with a 2° wide strip in galactic latitude between longitudes of $300^{\circ} \leqslant l \leqslant 60^{\circ}$ (Contreras et al. 2013). Also, the *Herschel Space Observatory* survey, Hi-Gal, has mapped the Galactic plane at 70, 160, 250, 350, and 500 μm (Molinari et al. 2010a, 2010b; Elia et al. 2013). When the complete ATLASGAL and Hi-Gal survey source catalogs are released and are combined with the BGPS catalogs, the final source catalog will contain tens of thousands of embedded sites of star formation in the Milky Way.

The population of objects discovered in the BGPS, ATLASGAL, and Hi-Gal surveys include dense starless and star-forming cores at the closest distances, clumps (unresolved collections of cores), and clouds at the farthest distances (Dunham et al. 2011a). In order to study the physical properties (e.g., size, mass, luminosity) of these embedded star-forming regions, their distances must first be determined. Distances in the Galactic plane may be derived using the Galactic rotation curve and a measurement of the source v_{LSR}. In the second and third quadrants, kinematic distances are uniquely determined; but, in the first and fourth quadrants, each measured v_{LSR} corresponds to both a near and far kinematic distance resulting in a kinematic distance ambiguity (KDA) that must be resolved using additional information.

Assignment of kinematic distances first and foremost requires a determination of the unique v_{LSR} of the 1.1 mm clump. CO is too easily excited in low density molecular gas to be a unique kinematic probe ($n_{eff} < 10^2$ cm^{-3}).[8] Along lines-of-sight that cross multiple arms of the Galaxy, as often happens in the first quadrant of the Galaxy, CO 1–0 emission displays complicated spectral shapes with multiple components spanning many tens of km s^{-1}. The gas directly associated with the clumps is best probed by a dense molecular gas tracer. Schlingman et al. (2011) performed a pilot survey of slightly less than 1/3 of the BGPS clumps (1882 sources) in the first and second quadrant of the

[8] The effective excitation density, n_{eff}, is defined as the density for which a $T_R = 1$ K line would be observed (see Evans 1999 for assumptions and Table 1 of Reiter et al. 2011a).

Galactic plane in the dense gas tracers HCO^+ and N_2H^+ 3–2 ($n_{\rm eff} \sim 10^4$ cm^{-3}). They showed that HCO^+ and N_2H^+ 3–2 are unique kinematic tracers of BGPS clumps with less than 2% of sources observed displaying multiple velocity components. They also resolved the KDA of a small subset ($N = 529$) of the BGPS clumps. Schlingman et al. (2011) found a median radius of 0.75 pc, a median mass of 320 $M_\odot$, a median volume density of 2400 cm^{-3}, and a median gravitational free-fall time of 750,000 years for this subset of sources. The resulting clump mass distribution ($dN/d\log M$) had a slope of −0.8 that is intermediate between the CO cloud mass distribution (−0.5; Solomon et al. 1987) and the Salpeter IMF (−1.35; Salpeter 1955; Scalo 1986) and is consistent with simulations of the fragmentation of turbulent compressible gas with a Kolmogorov spectrum (i.e., Hennebelle & Falgarone 2012). Schlingman et al. also observed a breakdown in the size line width relation in the dense molecular gas probed by HCO^+, possibly due to turbulent feedback on small scales from embedded protostellar sources (see Murray 2011). While the Schlingman survey provided an initial look the physical properties of BGPS clumps, the physical properties derived from the known distance sample in that paper represents less than 10% of the full BGPS v1.0.1 catalog and is biased toward the brightest 1.1 mm sources.

In this paper, we complete the spectroscopic observations started by Schlingman et al. (2011) and provide a complete spectroscopic catalog of observations of dense molecular gas as traced by HCO^+ and N_2H^+ 3–2 for all 6194 sources in the BGPS v1.0.1 catalog between $7.^\circ5 \leqslant l \leqslant 194^\circ$. We characterize the properties of the molecular emission ($v_{\rm LSR}$, I, Δv, etc.) for the spectroscopic catalog in this paper. A companion paper develops a Bayesian method for resolving the KDA for a subset of sources in the first quadrant by deriving distance probability density functions (DPDFs; Ellsworth-Bowers et al. 2013). The observing and calibration procedures are explained in Section 2, detection statistics are described in Section 3, and the source $v_{\rm LSR}$ are extracted in Section 4.1. The properties of the molecular emission are analyzed in Sections 4.2–4.5.

2. OBSERVATIONS

2.1. HHT Setup and Calibration

In the range $7.^\circ5 \leqslant l \leqslant 194^\circ$ 4705 BGPS clumps were observed during 51 observing shifts between 2011 February 28 and 2012 December 8 with the 10 m Heinrich Hertz Telescope (HHT).[9] The source catalog was determined by observing all Bolocat v1.0.1 sources that were not previously observed by Schlingman et al. (2011) plus re-observing sources where the pointing in Schlingman et al. exceeded half the HHT beamwidth (15″) from the v1.0.1 catalog peak 1.1 mm continuum position. Re-observation of a subset (393) of the Schlingman sources was necessary because the Schlingman et al. observations did not have access to the final v1.0.1 catalog positions, but were instead observed with an earlier (v0.7) version of the Bolocat (see Section 2.2). The observations in this paper are ultimately combined with the Schlingman et al. observations for sources with good correspondence to the v1.0.1 positions ($\Delta\theta < 15''$). The resulting spectroscopic catalog is a complete set of observations of every source (6194) in the v1.0.1 Bolocat with $7.^\circ5 \leqslant l \leqslant 194^\circ$.

The HHT observational procedure was similar to that used to observe the initial sample of 1882 BGPS clumps in Schlingman et al. (2011). Observations were performed with the 1 mm prototype-ALMA dual polarization, sideband-separating receiver. The receiver was tuned to HCO^+ 3–2 (267.5576259 GHz) in the lower sideband (LSB) and to N_2H^+ 3–2 (279.5118379 GHz) in the upper sideband (USB). Rejection between the sidebands was measured by observing the bright Galactic source, W75(OH), for 10 minutes each observing shift. The median rejections for the USB were −15.7 dB and −8.6 dB for vertical and horizontal polarization respectively. The 4-IF output was connected to one set of filterbanks with 1 MHz spectral resolution and 512 MHz bandwidth. This spectral resolution corresponds to a velocity resolution of 1.12 km s^{-1} in the LSB and 1.07 km s^{-1} in the USB. Each source was observed in position-switching mode with 1 minute of ON-source integration time. Emission free OFF positions for every half-degree of the galactic plane were determined by Schlingman et al. (2011).

Observations at the HHT are placed on the T_A^* scale using the standard Chopper-Wheel Calibration method (Penzias & Burrus 1973). Observations of planets are then used to determine the main beam efficiency and put the spectra on a final $T_{\rm mb}^{\rm pol} = T_A^*/\eta_{\rm mb}\eta_{\rm pol}$ scale, where $\eta_{\rm mb}\eta_{\rm pol}$ is the product of the telescope main beam efficiency and the coupling efficiency between the receiver optics for each polarization and the telescope. Unfortunately, during the bulk of the observing (47 out of 51 shifts), the only planet available for observation was Saturn. Saturn has two potential problems for calibration. First, the rings contribute to the 1.1 mm continuum and also block continuum from the planet. Fortunately though, the rings were oriented with inclinations between $7.^\circ3$ and $9.^\circ8$ which correspond to the shallow minimum in the millimeter brightness temperature (Weiland et al. 2011). Second, Saturn also has pressure broadened PH_3 $J_K = 1_0$–0_0 emission at 267 GHz in the atmosphere (Encrenaz & Moreno 2002). The LSB (HCO^+ 3–2) calibration is strongly affected by this absorption and cannot be used to calibrate the main beam efficiency. The USB (N_2H^+ 3–2) is much less affected by PH_3 absorption and was used to calibrate the USB main beam efficiencies. Jupiter was available for observations only after 2011 June and the ratio between LSB and USB efficiencies was applied to the Saturn calibration to derive the LSB main beam efficiencies.

As a consistency check, we also observed the source W75(OH) during every shift. The integrated intensity of W75(OH) correlates with the main beam efficiency measured using Saturn (Figure 1). A significant jump in the calibration is seen for both Saturn and W75(OH) at MJD = 55675 days. This discontinuity is due to a warmup of the receiver and subsequent adjustment of the feedhorn optics. The increase in efficiencies at this date occurs for all polarizations and sidebands simultaneously. The main beam efficiencies used in this paper are listed in Table 1. The final calibration numbers agree well with those used in Schlingman et al. The final spectrum is the baseline rms weighted-average of the calibrated vertical and horizontal polarizations $T_{\rm mb} = (T_{\rm mb}^{\rm Vpol}/\sigma^2_{T_{\rm mb}^{\rm Vpol}} + T_{\rm mb}^{\rm Hpol}/\sigma^2_{T_{\rm mb}^{\rm Hpol}})/(1/\sigma^2_{T_{\rm mb}^{\rm Vpol}} + 1/\sigma^2_{T_{\rm mb}^{\rm Hpol}}))$.

2.2. A Note About BGPS Catalog Versions

A spectroscopic survey of a large number of sources, such as the one presented in this paper, requires using a fixed source catalog during the course of the survey. At the start of the Schlingman et al. (2011) observations in 2008 November, the final BGPS v1.0 source catalog had not been completed, so Schlingman et al. utilized the preliminary Bolocat v0.7 catalog.

[9] The Heinrich Hertz Submillimeter Telescope is operated by the Arizona Radio Observatory.

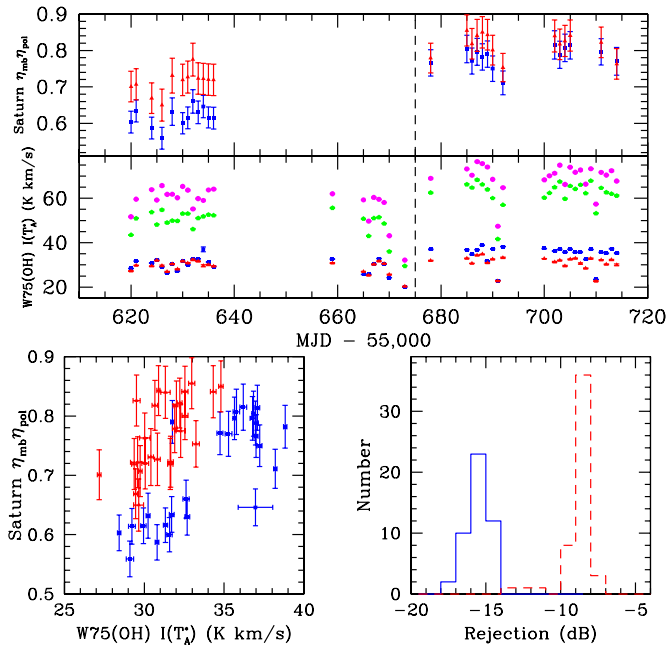

Figure 1. Top: the main beam efficiency of the USB measured on Saturn and the integrated intensity of HCO^+ 3–2 (LSB) and N_2H^+ 3–2 (USB) emission observed toward W75(OH) for Hpol USB (blue squares), Vpol USB (red triangles), Hpol LSB (green pentagons), and Vpol LSB (magenta circles). Due to PH_3 absorption in Saturn's atmosphere in the LSB, we only plot USB data for Saturn. The dashed line MJD-55,000 = 675 corresponds to a systematic change in the calibration associated with a warmup and adjustment of the receiver optics. Bottom left: the USB main beam efficiency of Saturn is well correlated with integrated intensities measured for W75(OH). Bottom right: histograms of the sideband rejection in the USB for Hpol (blue solid line) and Vpol (red dashed line).

Table 1
Calibration Efficiencies

MJD Range	η_{LSB}^{Vpol}[a]	η_{LSB}^{Hpol}	η_{USB}^{Vpol}	η_{USB}^{Hpol}	Catalog[b]
54863–54916	0.81 (0.04)	0.70 (0.03)	0.81 (0.03)	0.70 (0.04)	1
54917–54919	0.64 (0.01)	0.64 (0.01)	0.64 (0.02)	0.64 (0.02)	1
54920–54997	0.81 (0.04)	0.70 (0.03)	0.81 (0.03)	0.70 (0.04)	1
55620–55669	0.66 (0.03)	0.56 (0.03)	0.71 (0.03)	0.62 (0.03)	2
55678–56216	0.83 (0.03)	0.75 (0.03)	0.82 (0.03)	0.78 (0.03)	2

Notes.
[a] $\eta_{SB}^{pol} = \eta_{mb}\eta_{pol}$.
[b] Catalog number 1 = Schlingman et al. (2011) and 2 = new observations presented in this paper.

The results from those early spectroscopic observations helped tune the inputs for the seeded-watershed algorithm ultimately used to generate the v1.0 catalog (Rosolowsky et al. 2010). At the beginning of this current survey in 2011 February, the version 1.0.1 catalog was the latest version of the BGPS source catalog available and forms the basis for this paper. In 2013 February, a re-reduction of the BGPS (version 2.0) became available (Ginsburg et al. 2013). Simulations and testing of the new pipeline reduction plus characterization of the BGPS v2.0 angular transfer function are reported in Ginsburg et al. (2013). The resulting v2.0 BGPS maps recover larger scale structure better than v1.0 maps. A new v2.0 source catalog using the same inputs for the seeded-watershed algorithm that was used to generate the v1.0.1 catalog is also now available; however, the source selection algorithm has not been optimized for the noise structure in the new v2.0 maps. The fluxes quoted throughout this paper are derived from the new v2.0 BGPS 1.1 mm images. Since these new data products only became available after spectroscopic observations were completed (2012 December), we shall reference all spectroscopic observations sequentially in this paper to the v1.0.1 source names and catalog numbers in the spectral properties table (Tables 2 and 3).

3. DETECTION STATISTICS

The complete spectroscopic survey reaches a mean baseline rms of 58 mK for spectra in the LSB and 62 mK for spectra in the USB. As a result, the mean $3\sigma_{T_{mb}}$ limits for HCO^+ 3–2 and N_2H^+ 3–2 in this survey are 0.174 K and 0.186 K respectively. During the best weather, baseline rms of 30 mK were observed. The distribution of $\sigma_{T_{mb}}$ with Galactic longitude is shown in Figure 2.

Detections are confirmed visually, independently in each polarization, before the final spectrum is flagged. We adopt the flagging scheme in Schlingman et al. (2011) with two changes. We have eliminated the flag for large line wings (flag = 4 in the Schlingman et al. scheme); sources in the Schlingman catalog with a flag of 4 have been re-classified with a flag of 1 (single peak detection) or 3 (self-absorbed profile) in the final catalog presented in this paper. Also, to eliminate numerical gaps in our flag scheme, we have re-classified all self-absorbed profiles in the Schlingman et al. catalog (originally a flag of 5) as a flag of 3. The flags in the merged catalog span from 0 to 3 and correspond to: a source with a flag = 1 indicates a single v_{LSR} component detected at the $> 3\sigma_{T_{mb}}$ level; a source with a flag = 2 indicates a multiple v_{LSR} components detected; a source with a flag = 3

Table 2
HCO^+ 3–2 Observed Properties

Number	Source	α(J2000.0) (h:m:s)	δ (d:m:s)	Catalog[a]	Flag	v_{LSR} (km s^{-1})	T_{mb}^{pk} (K)	$\sigma_{T_{mb}}$ (K)	$I(T_{mb})$ (K km s^{-1})	σ_I (K km s^{-1})	Δv (km s^{-1})	$\sigma_{\Delta v}$ (km s^{-1})	FWZI (km s^{-1})
1307	G007.501+00.001	18:02:30.0	−22:28:07.0	2	0	...	...	0.095	...	...	...	...	...
1308	G007.507−00.255	18:03:28.7	−22:35:22.3	2	0	...	...	0.104	...	...	...	...	...
1309	G007.509+00.403	18:01:00.4	−22:15:46.3	2	1	7.5	0.450	0.086	1.245	0.288	2.7	0.5	...
1310	G007.564−00.042	18:02:47.8	−22:26:05.6	2	0	...	...	0.070	...	...	...	...	...
1311	G007.600−00.142	18:03:15.0	−22:27:10.1	2	1	153.3	0.477	0.061	1.384	0.235	3.4	0.4	3.4
1312	G007.622+00.002	18:02:45.3	−22:21:45.8	2	0	...	...	0.081	...	...	...	...	...
1313	G007.622−00.000	18:02:45.8	−22:21:49.4	2	0	...	...	0.080	...	...	...	...	...
1314	G007.632−00.110	18:03:11.9	−22:24:33.1	2	1	153.9	2.254	0.066	13.348	0.290	6.2	0.2	11.2
1315	G007.636−00.150	18:03:21.4	−22:25:31.4	2	1	154.8	0.519	0.060	1.412	0.200	2.7	0.3	3.4
1316	G007.636−00.194	18:03:31.4	−22:26:49.4	2	1	152.6	1.167	0.055	6.192	0.248	5.5	0.2	10.1

Notes. [a] Catalog number 1 = Schlingman et al. (2011) and 2 = new observations presented in this paper.
(This table is available in its entirety in a machine-readable form in the online journal. A portion is shown here for guidance regarding its form and content.)

Table 3
N_2H^+ 3–2 Observed Properties

Number	Source	Catalog[a]	Flag	v_{LSR} (km s^{-1})	T_{mb}^{pk} (K)	$\sigma_{T_{mb}}$ (K)	$I(T_{mb})$ (K km s^{-1})	σ_I (K km s^{-1})	Δv (km s^{-1})	$\sigma_{\Delta v}$ (km s^{-1})	FWZI (km s^{-1})
1307	G007.501+00.001	2	0	...	...	0.113	...	...	...	...	...
1308	G007.507−00.255	2	0	...	...	0.097	...	...	...	...	...
1309	G007.509+00.403	2	0	...	...	0.093	...	...	...	...	...
1310	G007.564−00.042	2	0	...	...	0.078	...	...	...	...	...
1311	G007.600−00.142	2	1	153.0	0.404	0.082	1.979	0.308	...	...	...
1312	G007.622+00.002	2	0	...	...	0.067	...	...	...	...	...
1313	G007.622−00.000	2	0	...	...	0.078	...	...	...	...	...
1314	G007.632−00.110	2	1	153.9	1.591	0.079	7.967	0.339	5.3	0.2	8.6
1315	G007.636−00.150	2	1	155.3	0.661	0.068	1.633	0.224	2.5	0.3	4.3
1316	G007.636−00.194	2	1	152.8	0.858	0.086	4.679	0.380	4.9	0.3	6.4

Notes. [a]Catalog number 1 = Schlingman et al. (2011) and 2 = new observations presented in this paper.
(This table is available in its entirety in a machine-readable form in the online journal. A portion is shown here for guidance regarding its form and content.)

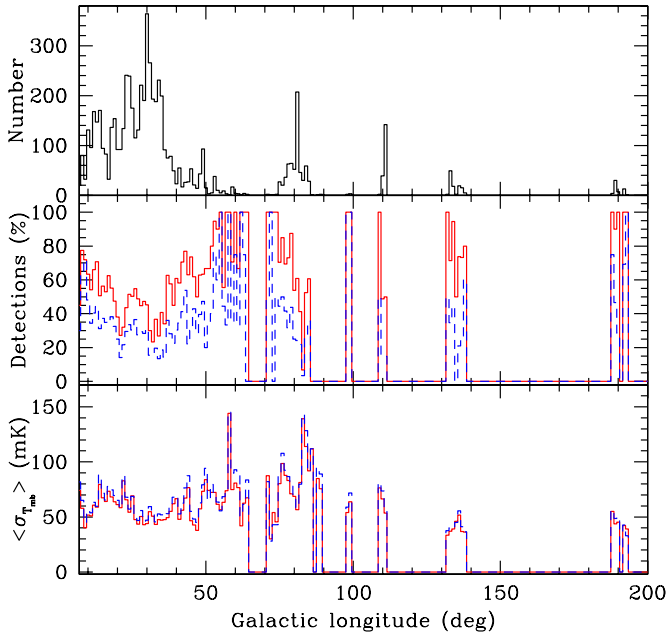

Figure 2. Top: the distribution of BGPS v1.0.1 catalog sources with Galactic longitude. Middle: detection fraction for each Galactic longitude bin of HCO^+ 3–2 (solid red histogram) and N_2H^+ 3–2 detections (dashed blue histogram). Bottom: the distribution of the average baseline rms for HCO^+ 3–2 (red, solid line) and N_2H^+ 3–2 (blue, dashed line). Values of zero indicate l ranges with no sources. $\langle\sigma_{T_{mb}}\rangle$ = 58 mK for HCO^+ 3–2 and $\langle\sigma_{T_{mb}}\rangle$ = 62 mK for N_2H^+ 3–2 for the complete spectroscopic survey.
(A color version of this figure is available in the online journal.)

indicates a source with possible self-absorption; and a source with a flag = 0 indicates a non-detection.

Examples of spectra with different flag combinations are shown in Figure 3. The vast majority of detections are similar to source 3054 (G23.370+0.140) with a single Gaussian peak in both HCO^+ and N_2H^+ 3–2 (HCO^+ flag = 1 and N_2H^+ flag = 1). Source 1315 (G07.636−0.150) is an example of a N_2H^+ detection that is stronger than a HCO^+ detection while source 6620 (G78.233−0.347) is an example of a HCO^+ detection and a N_2H^+ non-detection. Source 2060 (G14.540−0.210) is an example of a non-detection in both lines over the full velocity range permissible for objects at $l = 14^\circ$ (−60 to +160 km s^{-1}). The four panels on the right of Figure 3 display examples of detections with multiple velocity peaks. Source 3244 (G24.143+0.128) shows two clearly separated velocity peaks ($\Delta v_{LSR} = 60$ km s^{-1}) indicative of two physically separate dense clumps along the same line-of-sight. Occasionally, the two peaks are blended. In the case of source 2162 (G15.079−0.604), the N_2H^+ 3–2 spectrum peaks at the same velocity as one of the HCO^+ 3–2 peaks; therefore, we do not classify this source as a self-absorbed profile, but as multiple velocity components in HCO^+ 3–2 (HCO^+ flag = 2). The two panels on the bottom right of Figure 3 show examples of blue-skewed and red-skewed self-absorbed HCO^+ 3–2 profiles where the N_2H^+ 3–2 emission does peak near the self-absorption minima (HCO^+ flag = 3).

The detection fractions for each spectroscopic flag are summarized in pie charts in Figure 4. HCO^+ 3–2 emission was detected toward a total of 3206 (51.8%) sources. N_2H^+ 3–2 emission was detected toward a smaller fraction, 1878 (30.3%) sources. Multiple velocity components are rare in these dense gas tracers with 84 HCO^+ 3–2 multiple velocity detections (1.3%) and 32 N_2H^+ 3–2 multiple velocity detections (0.5%). There are only four N_2H^+ 3–2 detections (0.06%) that lack a corresponding HCO^+ 3–2 detection. None of these four unique N_2H^+ 3–2 detections are very significant, only ranging from $T_{mb}^{pk} = (3–5)\sigma_{T_{mb}}$. As an example, source 1705 (G012.387+00.230) has a 3.7σ detection in T_{mb} for N_2H^+ 3–2 but there is a potential HCO^+ 3–2 detection at only 2.9σ which falls just short of the criteria set in this paper for a HCO^+ detection flag = 1. Strong N_2H^+ 3–2 emission without an HCO^+ 3–2 detection does not occur for the BGPS sources observed in this spectroscopic catalog. Therefore, we have observed a unique velocity component for 3126 sources (50.5%) in the Bolocat v1.0.1 within the range $7.^\circ5 \leqslant l \leqslant 194^\circ$.

The distributions of T_{mb} for both tracers are shown in Figure 5. Both histograms peak just above the $3\sigma_{T_{mb}}$ limit indicating that deeper integration is likely to detect more sources in the lines of HCO^+ and N_2H^+ 3–2. The total observing time for the complete spectroscopic survey is >600 hr; a modest decrease of a factor of two in the rms noise level would require four times longer than the current survey. The detection statistics are a function of Galactic longitude in this survey (see Figure 2). The detection fraction does not strongly correlate with the baseline rms in the survey (Figure 5). For instance, the region near $l = 30^\circ$ which has the largest number of 1.1 mm sources within a 1° bin has a detection fraction of only 30% despite having small baseline rms compared to the entire survey ($\sigma_{T_{mb}} = 40$ mK). An opposite example can be found at $l = 83^\circ$ where a higher baseline rms results in a lower detection fraction; however, these instances are rare in this survey.

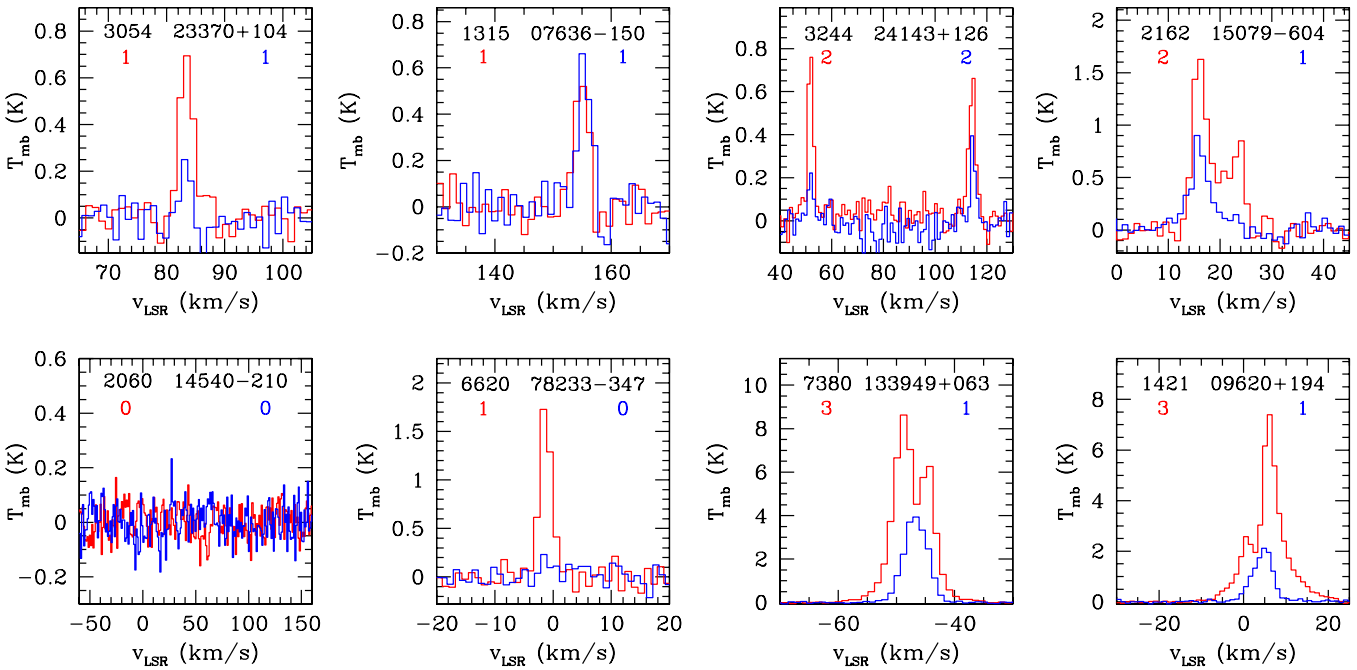

Figure 3. Example spectra showing different flag combinations. Red spectra are HCO^+ 3–2 and blue spectra are N_2H^+ 3–2. The Bolocat v1.0.1 source number is listed in the upper left of each panel while the truncated v1.0.1 catalog source name is listed in the top right of each panel. The HCO^+ 3–2 flag is shown in red below the source number on the left while the N_2H^+ 3–2 flag is shown in blue below the source name on the right. The majority of detections are similar to source 3054 (G23.370+0.104). Source 1315 (G07.636−0.150) is an example of a N_2H^+ brighter source. Source 6620 (G78.233−0.347) is an example of a HCO^+ detection and a N_2H^+ non detection. Source 2060 (G14.540−0.210) is a non detection in both lines. Note that the velocity scale for the non-detection source 2060 spans the full range of plausible v_{LSR} for a source at $l = 14.^{\circ}5$. The spike near 30 km s^{-1} in the G14.540−0.210 N_2H^+ spectrum is not a detection as it is only one channel wide and does not appear independently in both polarizations. Sources 3244 (G24.143+0.126) and 2162 (G15.079−0.604) show examples of multiple v_{LSR} components where N_2H^+ peaks in one or both velocity components. The two self-absorbed profiles (sources 7380 and 1421) show examples of blue and red asymmetries in the HCO^+ 3–2 profiles, respectively, with the N_2H^+ 3–2 spectra peaking near the self-absorption minima.

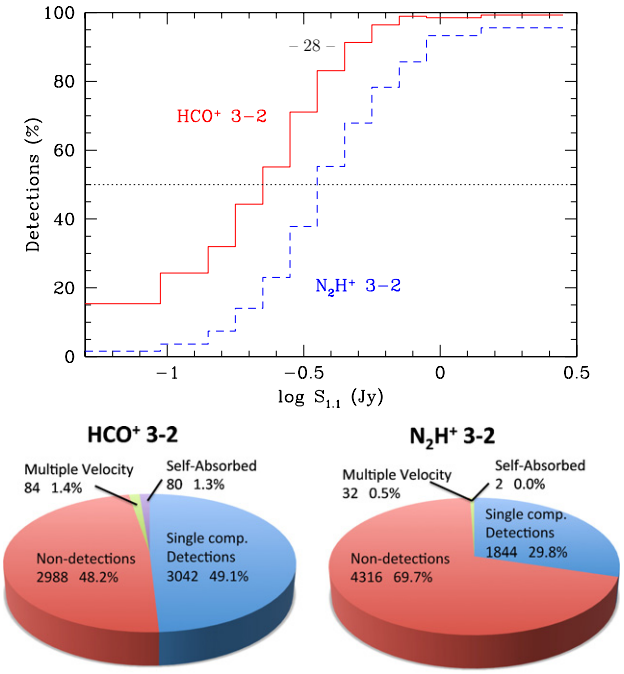

Figure 4. Top: the detection fraction for HCO^+ 3–2 (red solid line) and N_2H^+ 3–2 (blue dashed line) vs. 1.1 mm flux densities derived from the v2.0 BGPS maps at the location of the HHT pointing position. The HCO^+ 3–2 detection fraction is above 50% for 1.1 mm flux densities > 200 mJy. Bottom: detection flag statistics for HCO^+ and N_2H^+ 3–2 for 6194 sources in the complete spectroscopic catalog.

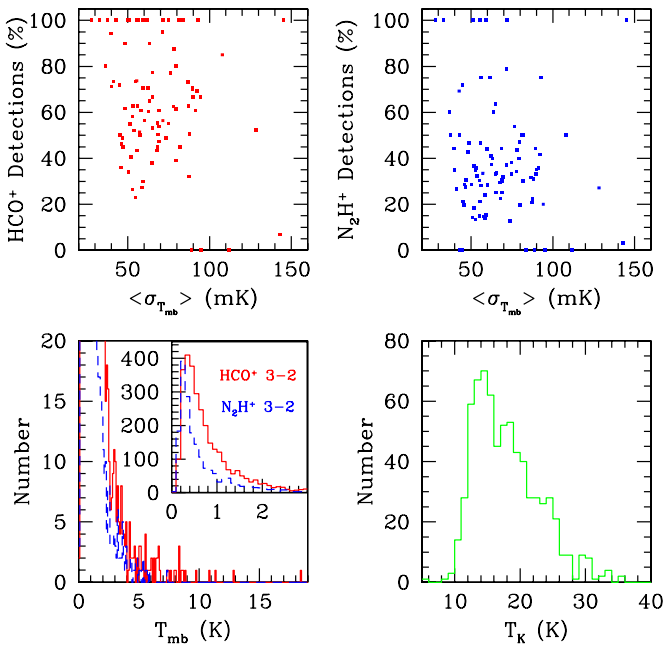

Figure 5. Top panels: the HCO^+ 3–2 (LEFT) and N_2H^+ 3–2 (right) detection fraction plotted vs. average baseline rms per 1° bin in Galactic longitude. Bottom left: the main beam brightness temperature for HCO^+ 3–2 (red solid line) and N_2H^+ 3–2 (blue dashed line). We have truncated the histograms at 3K to better display the peak of each distribution. Bottom right: the histogram of gas kinetic temperature from the overlap NH_3 sample.

In order to understand this result, we must first compare the detection statistics to the flux density of BGPS sources. The detection fraction is a strong function of the 1.1mm flux density of BGPS sources (Figure 4). v1.0.1 sources with 1.1mm flux densities below 200 mJy have a less than 50% detection percentage with the detection fraction decreasing rapidly below this flux density. This flux density corresponds to a column density limit of $N_{\rm H_2} = 4 \times 10^{21}$ cm^{-2} assuming a dust temperature of 20 K, gas mass to dust mass ratio of 100:1, and Ossenkopf & Henning opacities ($\kappa_{1.1}^{\rm OH5} = 1.14$ cm^2 g^{-1}; Ossenkopf & Henning 1994). In contrast, sources with flux densities above 500 mJy have a detection fraction approaching 90% ($N_{\rm H_2} \geqslant 1 \times 10^{22}$ cm^{-2}). These variations in detection fraction with Galactic longitude primarily represent variations in the number of low flux density sources selected by the Bolocat seeded-watershed algorithms in different, sometimes crowded, regions of the Galactic plane (see Figure 17 of Rosolowsky et al. 2010). The region toward $l = 30^\circ$ contains a larger fraction of low flux density ($S_{1.1} < 200$ mJy) sources than other regions in the Galactic plane resulting in the lower overall detection fraction. This $l = 30^\circ$ region of the Galactic plane is crowded and confused as the observed line-of-sight crosses the Sagittarius arm, the tangent of the end of the molecular bar, Perseus arm, and an outer Galactic arm.

We can test the fidelity of low flux density sources in the v1.0.1 catalog by directly comparing to the detection statistics with the new v2.0 catalog. For sources with no v2.0 catalog counterpart within 60″ of the v1.0.1 source position (1813 sources), the HCO$^+$ 3–2 non-detection fraction (HCO$^+$ flag = 0) increases from 48.0% for the complete v1.0.1 catalog to 73.7% for this subset. Nearly half of all v1.0.1 HCO$^+$ 3–2 non-detections are no longer directly associated with sources in the v2.0 catalog. Furthermore, those v1.0.1 sources that lack a v2.0 counterpart are predominantly low flux density v1.0.1 sources (Ginsburg et al. 2013) A significant fraction of low flux density v1.0.1 sources may not be real or are low volume density sources at the limit of statistical significance in the 1.1 mm map. Conversely, there are 476 v1.0.1 sources which have HCO$^+$ 3–2 detections (HCO$^+$ flag = 1 or 3) but no nearby (< 60″) counterpart in the v2.0 catalog. These results indicate that the v2.0 catalog has a better chance of selecting clumps with detectable dense molecular gas (at the limit of this spectroscopic survey) but that the v2.0 catalog is incomplete and misses a significant number of sources with dense molecular gas in the BGPS survey. This comparison only serves to highlight the difficulties inherent in source selection algorithms and also how surveys of dense molecular gas may be used to test the fidelity of those source catalogs.

4. PROPERTIES OF MOLECULAR DETECTIONS

In this section, we analyze the properties of the HCO$^+$ and N$_2$H$^+$ 3–2 emission for the complete set of 3210 spectroscopic detections. The spectra are analyzed using the same analysis techniques presented in Schlingman et al. (2011). Namely, a single component Gaussian is fit to HCO$^+$ 3–2 spectra while a multiple-component hyperfine fit is performed on N$_2$H$^+$ 3–2 spectra. In cases where a single component Gaussian fit fails or is not appropriate to described the observed line shape, the velocity of $T_{\rm mb}^{\rm pk}$ is reported. The integrated intensities ($I = \int T_{\rm mb} dv$) are determined from direct integration of the spectra. Tables 2 and 3 list the derived spectroscopic properties ($\sigma_{T_{\rm mb}}$, $v_{\rm LSR}$, $T_{\rm mb}^{\rm pk}$, I, FWHM, and FWZI) for HCO$^+$ and N$_2$H$^+$ 3–2 observations of all 6194 sources in the v1.0.1 catalog with $7.^\circ5 \leqslant l \leqslant 194^\circ$.

In addition to the molecular lines observed in this survey, NH$_3$ is another popular dense gas tracer because it is easily excited in dense molecular gas and the ratio of the (1,1) and (2,2) inversion lines may be used to determine the gas kinetic temperature (Ho & Townes 1983). There have been two substantial Galactic NH$_3$ surveys published in the past two years. The Dunham et al. (2011b) survey used the 100 m Green Bank Telescope (GBT) to follow-up a sample of 631 BGPS sources in the (1,1), (2,2), and (3,3) inversion lines. The Wienen et al. (2012) survey used the 100 m Effelsberg Telescope (of which the inner 80 m is practical for 1 cm NH$_3$ observations) to follow up 862 ATLASGAL sources in the (1,1) and (2,2) inversion lines. We have directly compared the positions observed in the Dunham et al. and Wienen et al. NH$_3$ catalogs with the HHT pointing positions to find a subset of 546 sources with NH$_3$ pointings within 15″ and having both published NH$_3$ detections and HCO$^+$ 3–2 detections. The distribution of gas kinetic temperatures for these 546 sources is shown in Figure 5. The median is $T_k = 18.3$ K with a positively skewed tail of kinetic temperatures. We shall also use the gas kinetic temperature from this overlap subset of 546 sources in the subsequent analysis.

4.1. Kinematics of BGPS Sources

The primary purpose of this spectroscopic survey is to find a unique $v_{\rm LSR}$ for each BGPS source. The $v_{\rm LSR}$ for molecular detections is determined from a Gaussian fit to the HCO$^+$ 3–2 line for sources with a flag = 1. Observations of N$_2$H$^+$ 3–2, when detected, provide an independent measurement of the velocity of dense molecular gas.

Figure 6 plots the distribution of 3126 observed velocities with Galactic longitude overlaid on the CO 1–0 integrated intensities map from the Dame et al. (2001) survey. The BGPS clumps generally follow the regions of strong CO 1–0 emission and trace major kinematic features in the Galaxy. The most prominent concentration of sources exists at $l \sim 30^\circ$ and $v_{\rm LSR} \sim +90$ km s^{-1} corresponding to the tangent to the molecular ring and the central molecular bar. This also corresponds to a secondary maximum in the Galactic longitude distribution of sources in the first quadrant (Aguirre et al. 2011; Beuther et al. 2012) with the peak of that distribution being toward $l = 0^\circ$. The second most prominent kinematic feature is the molecular ring which extends diagonally in Figure 6 from $l = 30^\circ$ to the longitude limit in this survey ($l = 7.^\circ5$). The vast majority of sources between $l = 7.^\circ5$ and $l = 30^\circ$ are associated with this structure in the Milky Way. Unfortunately, these sources suffer from the KDA within the molecular ring which becomes more severe as Galactic longitude decreases from the tangent point with the bar near $l = 30^\circ$. BGPS clumps can be observed on the far side of the Galaxy as evinced by the sources tracing the CO-delineated outer extension of the Norma arm from $l = 25^\circ$ to 45° and $v_{\rm LSR} = -10$ to -50 km s^{-1}. Since the BGPS is confined to $\pm 0.^\circ5$ for most longitude ranges, the BGPS has difficulty tracing sources in the newly discovered outermost arm of the Milky Way (Dame & Thaddeus 2011) because the Galactic warp projects sources to Galactic latitudes greater than the typical $0.^\circ5$ extent of the BGPS. A secondary clump of sources is distinct toward $l \sim 80^\circ$ and $v_{\rm LSR} \sim 0$ km s^{-1} that are associated with the famous Cygnus OB associations and star-forming regions within the local arm (Reipurth & Schneider 2008).

The $v_{\rm LSR}$ of sources with both HCO$^+$ and N$_2$H$^+$ 3–2 detections are shown in Figure 6. The velocities of these two tracers

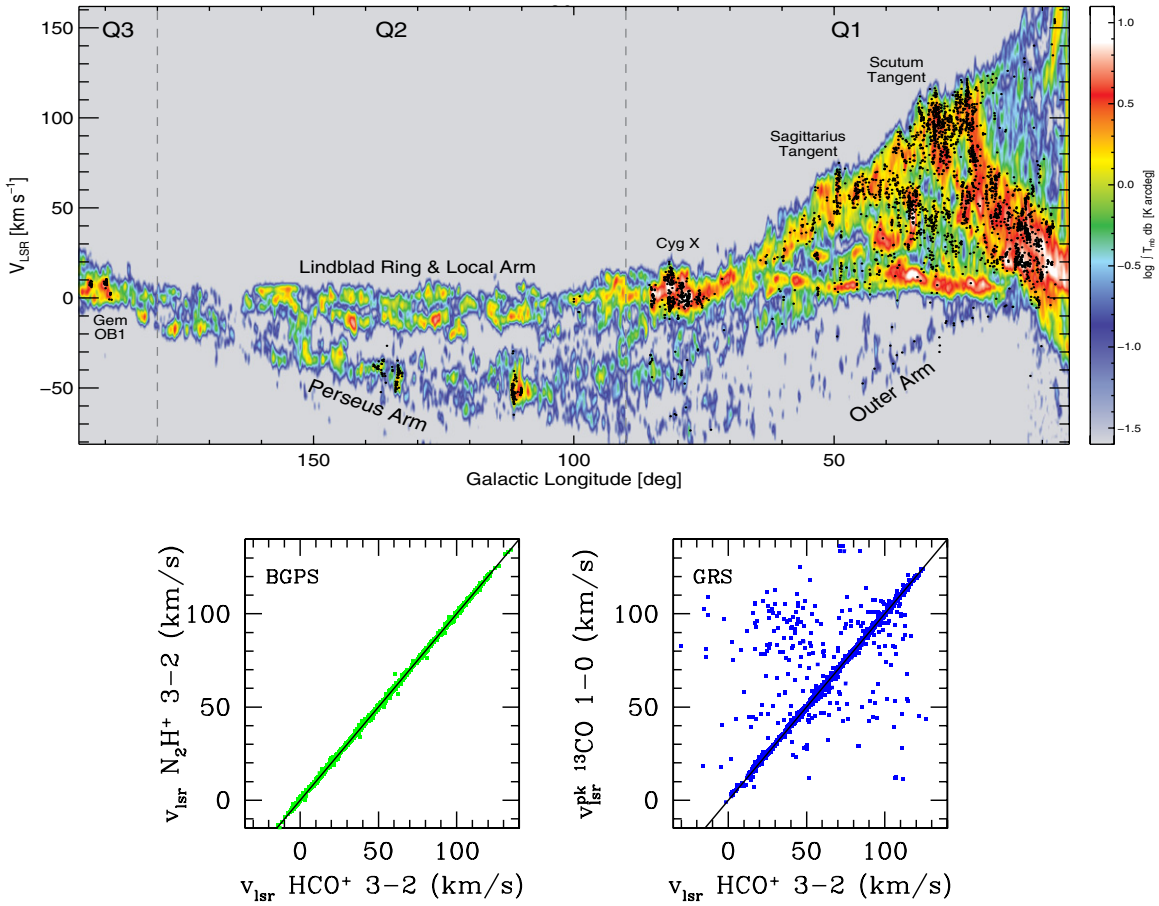

Figure 6. Top: velocities of BGPS clumps (black circles) overlaid on the CO 1–0 l-v diagram of the Milky Way from Dame et al. (2001). Bottom panels: (left) $v_{\rm lsr}$ of N_2H^+ 3–2 vs. HCO^+ 3–2 for BGPS clumps with single component detections in both lines. The black line is the 1:1 line. (right) $v_{\rm lsr}$ of ^{13}CO 1–0 vs. HCO^+ 3–2 for 1681 GRS sources that overlap BGPS molecular detections.

are very well correlated and centered on the one-to-one line. Since the N_2H^+ 3–2 spectra were reduced independently of the HCO^+ detections, this result indicates high fidelity of the $v_{\rm LSR}$ determined from the dense gas detections reported in this paper.

We also directly compare the $v_{\rm LSR}$ from our survey with the spectra that were observed within $15^\circ < l < 56^\circ$ by the ^{13}CO 1–0 Galactic Ring Survey (GRS; Jackson et al. 2006; Roman-Duval et al. 2009). GRS spectra are obtained for the v1.0.1 source positions from which the velocity of the peak $T_{\rm mb}$ were calculated. 1681 sources have both ^{13}CO 1–0 GRS spectra and a BGPS dense gas detection. The peak ^{13}CO 1–0 velocities agree within 2 km s^{-1} with BGPS velocities for 81.4% of the sources. There is a substantial number of sources with discordant velocities: 217 sources (12.9%) have a velocity offset > 7 km s^{-1}. As can be seen in the bottom right panel of Figure 6, many of these large discrepancies are tens of km s^{-1} and it would be unwise to blindly use the ^{13}CO 1–0 peak velocity to determine kinematic distances.

The comparison statistics improve slightly for the small subset of 141 sources observed by Eden et al. (2012) in the ^{13}CO 3–2 transition with 87.1% of sources with velocities that agree within 2 km s^{-1}. While the higher excitation CO transition does a slightly better job of picking the unique velocity of dense gas, ^{12}CO and ^{13}CO cannot be used to uniquely determine the velocities of all BGPS clumps. Observations in dense gas tracers (with a contamination rate from multiple components of only 1.3%) are required for certainty in determining $v_{\rm LSR}$ of a BGPS clump.

Many BPGS sources appear to be physically associated with complexes of sources. This is evident in the kinematic finder chart centered on $l = 10\overset{\circ}{.}75$, $b = -0\overset{\circ}{.}3$ (Figure 7). The BGPS v2.0 1.1 mm continuum images is displayed in greyscale with flux density indicated along the top. Sources with unique velocity detections are displayed as green circles with the $v_{\rm LSR}$ indicated above the source. Red crosses correspond to positions with no detection. Yellow diamonds correspond to sources with multiple velocity components. The brightest 1.1 mm complex in the southwest quadrant of Figure 7 ranges in velocity from -4.1 to -1.5 km s^{-1} and appears to be both spatially and kinematically connected. There is a second, weaker 1.1 mm complex to the northeast that ranges in velocity from +28.6 to +30.8 km s^{-1} that may be two vertical (aligned in Galactic latitude) filaments. Two sources at -5.3 and +51.0 km s^{-1} are clearly interlopers and are not associated once $v_{\rm LSR}$ is taken into account. This example highlights the need for kinematic information to determine whether objects might be associated.

A simple tool for analyzing whether sources are kinematically associated is to study the distribution of nearest neighbors to each spectroscopically detected source. We calculate the difference in velocity, $\Delta v_{\rm LSR}$, for the nearest neighbor for all single component molecular detections. The distribution of $\Delta v_{\rm LSR}$ is shown in Figure 8 for all nearest neighbor sources that are within 10′ (1516 sources). Just over 2/3 of nearest neighbors appear kinematically associated (69% of nearest neighbors have $\Delta v_{\rm LSR} < 7$ km s^{-1}). This is not a surprising result because multiple BGPS clumps may lie within the same molecular cloud

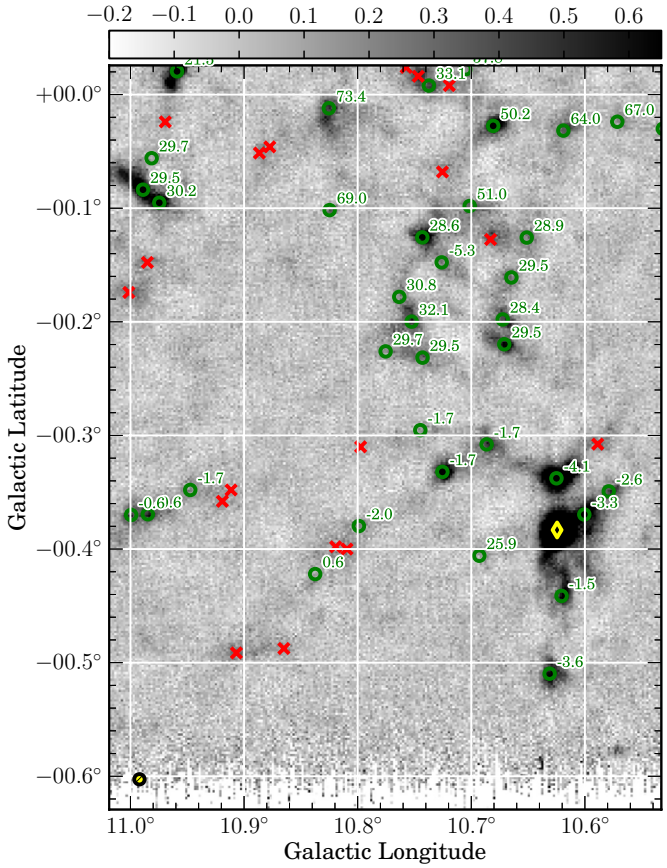

Figure 7. Example finder chart for the 0.°5 region centered on $l = 10.°75$ $b = -0.°3$. Velocities of BGPS clumps (km s^{-1}) overlaid on the BGPS 1.1 mm v2.0 continuum image. Green circles indicate a single v_{LSR} component detection, yellow diamonds indicate multiple v_{LSR} detected, and red crosses indicate no HCO^+ or N_2H^+ 3–2 detection. The gray scale is flux density in units of Jy. The Bolocam beam at 1.1 mm is shown as the filled yellow circle in the lower left.

(A color version of this figure is available in the online journal.)

traced by CO (e.g., Eden et al. 2012, 2013). Identifying physically connected clumps or filaments is difficult in the BGPS maps because of the spatial filtering due to atmospheric subtraction; however, observations from the *Herschel Space Observatory* will suffer less severe spatial filtering than ground-based observations. Early *Herschel* observations revealed a plethora of filaments within the Galactic plane (e.g., Men'shchikov et al. 2010; Molinari et al. 2010a, 2010b; Arzoumanian et al. 2011; Palmeirim et al. 2013). The kinematic information presented in this paper will be crucial for finding spatially and kinematically connected filaments in observations of the Galactic plane from the *Herschel Space Observatory*.

4.1.1. A Methodology for Deriving Heliocentric Distances

Ultimately, in order to derive physical properties of BGPS clumps such as size, mass, and luminosity, we must determine the heliocentric distances, $d_\odot$. For sources in the first quadrant, resolving the KDA presents a formidable problem. The top left panel of Figure 8 shows the distribution of the difference between the far and near heliocentric distance. The majority of sources observed in the first quadrant have $\Delta d_\odot = d_{far} - d_{near}$ that vary between 3–10 kpc. For physical quantities, such as the mass or the luminosity, that functionally depend on $d_\odot^2$, the resulting uncertainty are factors of one to two orders of magnitude.

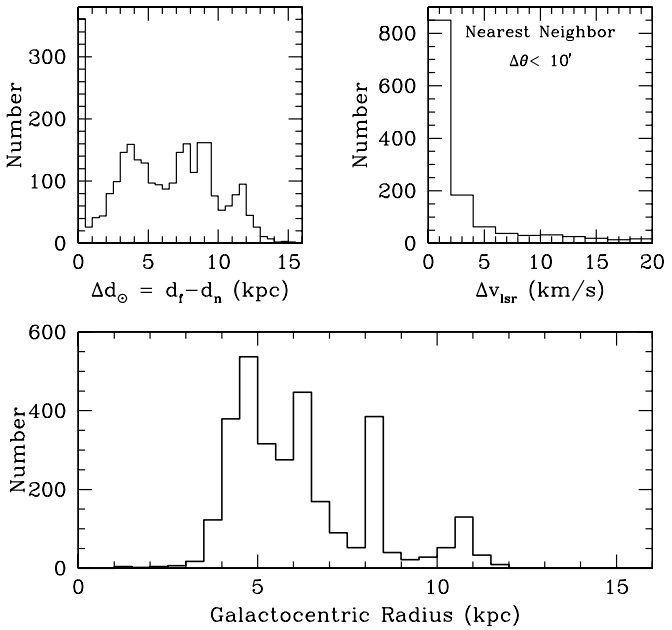

Figure 8. Top left: the distribution of the difference between the far and near kinematic distances. Top right: the distributions of nearest neighbor sources in Δv_{LSR} for neighbors that are within 10′. Bottom: the distribution of sources in Galactocentric radius. Peaks are clearly distinguished for the molecular ring, Sagittarius arm, local spur, and Perseus arm.

It is unlikely that we will be able to uniquely resolve the KDA for every spectroscopic detection in this catalog. A statistical approach is more appropriate to characterize the probability of finding a source at a given distance. The companion paper to this survey by Ellsworth-Bowers et al. (2013) develops a Bayesian technique for deriving the posterior distance probability density functions (DPDFs) for BGPS clumps. In this framework, the posterior distribution is given by the product of the likelihood function (derived from v_{LSR} and the rotation curve of the Galaxy) and prior distributions that constrain the probability of finding the source at near or far kinematic distances

$$\mathrm{DPDF}(d_\odot) = \mathcal{L}(v_{LSR}, l, b; d_\odot) \prod_i P_i(d_\odot, l, b). \quad (1)$$

The likelihood function, $\mathcal{L}(v_{LSR}, l, b; d_\odot)$, is a bimodal distribution with equal probability centered on the near and far kinematic distances derived from the Reid et al. (2009) rotation model of the Galaxy with a 7 km s^{-1} uncertainty (see Ellsworth-Bowers et al. 2013; Reid et al. 2009). Ellsworth-Bowers et al. (2013) develops two prior distributions based on the azimuthally averaged distribution of H_2 in the Galaxy (Wolfire et al. 2003) and a radiative transfer model of the Galactic 8 μm emission (Robitaille et al. 2012) to derive the DPDF for BGPS sources associated with 8 μm absorption features (EMAFs) observed in *Spitzer* images. This study shows that not all EMAFs can be automatically associated with the near kinematic distance; 15% of BGPS sources associated with EMAFs are placed at or beyond the tangent distance. Additional prior distributions (i.e., based on the presence or lack of H I absorption features; see Roman-Duval et al. 2009) may be used to further constrain the DPDFs. The distribution of a source property (i.e., size, mass, luminosity, etc.) may then be calculated using Monte Carlo techniques that marginalize over distance (randomly drawn from the DPDFs) and other relevant physical variables (i.e., dust temperature and dust opacity in the calculation of mass from the observed 1.1 mm flux; see Schlingman et al. 2011). Calculation of DPDFs

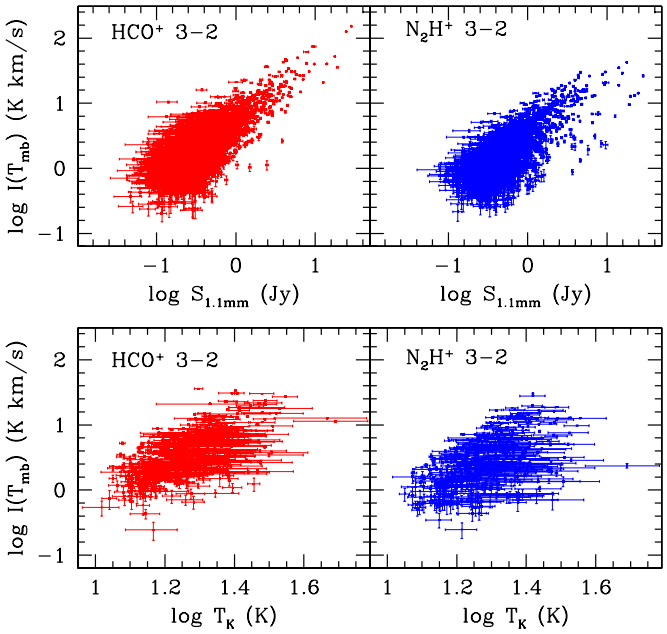

Figure 9. Integrated intensity of HCO^+ 3–2 (top left) and N_2H^+ 3–2 (top right) vs. 1.1 mm flux density from v2.0 maps. The integrated intensity of HCO^+ 3–2 (bottom left) and N_2H^+ 3–2 (bottom right) vs. gas kinetic temperature determined from NH_3 observations.

(A color version of this figure is available in the online journal.)

for the entire spectroscopic catalog is beyond the scope of this current paper and is the subject of ongoing work by the BGPS team.

There is no distance ambiguity for Galactocentric radius, R_{gal}. This permits us to compare the molecular derived properties versus R_{gal} for the subset of 3126 unique kinematic detections. The Galactocentric radius may be derived from the observed v_{LSR}, l, b, and the assumed rotation curve of the Galaxy ($v(r)$). We use the Reid et al. (2009) model for the rotation curve of the Milky Way determined from parallax measurements of maser sources. A *FORTRAN* program supplied by M. Reid (2009; private communication) calculates the near or far kinematic distances from observed v_{LSR} and galactic coordinates. The bottom panel of Figure 8 shows the distribution of sources with R_{gal}. Four distinct peaks are visible: the molecular ring at 4.5 kpc, the Sagittarius arm at 6.5 kpc, the Local arm at 8.5 kpc, and the outer Perseus arm at 10.5 kpc.

4.2. Molecular Intensity Comparisons

The brightest HCO^+ 3–2 sources have integrated intensities over 150 K km s^{-1}. The brightest HCO^+ 3–2 source, (6362 G49.489−0.370) is also the brightest 1.1 mm source and appears associated with the luminous infrared source W51 IRS2S (Wynn-Williams et al. 1974). Both the HCO^+ and N_2H^+ 3–2 spectra display a strong red asymmetry likely indicative of the strong molecular outflows in this region. The brightest N_2H^+ 3–2 source is 2152 (G015.013−00.674) with $I = 42.6$ K km s^{-1} and is associated with the M17–SW region.

Schlingman et al. (2011) reported a correlation between the HCO^+ and N_2H^+ 3–2 integrated intensities and the 1.1 m flux density for the subset of 1882 sources observed. The correlations for the complete spectroscopic catalog are plotted in Figure 9. Similar positive correlations are observed for both molecules (Pearson's product–moment correlation coefficient is $r_{corr} = 0.78$ for HCO^+ 3–2 and $r_{corr} = 0.75$ for N_2H^+ 3–2). The excellent overlap in points between new observations presented in this paper the Schlingman catalog indicates that the calibration between the two sets of observations is consistent (Section 2).

The bottom panels of Figure 9 also show a correlation between HCO^+ integrated intensity and kinetic temperature indicating that warmer sources have more HCO^+ 3–2 emission ($r_{corr} = 0.62$). N_2H^+ 3–2 emission is slightly less well correlated with T_k ($r_{corr} = 0.53$). There is, however, a tendency for N_2H^+ 3–2 emission to be brighter in warmer clumps. This is likely due to excitation conditions in those clumps. The $J = 3$ level is 26.8 K above ground and the level populations and subsequent intensity of the 3–2 line are sensitive to the gas kinetic temperature (see Section 4.4). It will be important to ultimately compare the 1–0 transitions, for instance from the MALT90 survey (Foster et al. 2011, 2013), to derive the chemical abundances of HCO^+ and N_2H^+ with less sensitivity to excitation conditions.

We also find positive correlations in the integrated intensities of HCO^+ and N_2H^+ 3–2 emission ($r_{corr} = 0.82$) and in the ratio $I_{line}/S_{1.1}$ ($r_{corr} = 0.62$; Figure 9). This ratio of integrated intensity to 1.1 mm flux density is linearly proportional to the molecular abundance if molecular emission is in the optically thin limit. We must caution that the assumption that HCO^+ and N_2H^+ 3–2 emission is optically thin is likely untrue for most BGPS sources and that optical depth effects will modify optically thin column densities by the factor $\frac{\tau}{1-\exp(-\tau)} \sim \tau$ for thick lines (see Section 4.4).

HCO^+ and N_2H^+ have opposite chemical behavior with respect to CO. HCO^+ is primarily formed in the gas phase from reactions of CO with H_3^+ while N_2H^+ is destroyed by gas phase CO (see Jørgensen et al. 2004). Since CO is adsorbed onto dust grains at high densities ($n > 10^4$ cm^3) and low temperatures ($T_k < 20$ K), the gas phase abundances of HCO^+ and N_2H^+ are expected to be anti-correlated in cold, dense, heavily CO-depleted environments. The correlations observed above seem to contradict the simple chemical expectation if they are naively interpreted as representing variations in the abundance of HCO^+ and N_2H^+. However, we must be careful when directly comparing integrated intensities since this quantity is function of both the column density (or abundance) and the excitation conditions, which play an important role for the 3–2 transitions (see Section 4.4).

A large ratio of N_2H^+/HCO^+ emission may be a better indicator of a significant reservoir of cold, dense gas within a BGPS clump. There are 113 sources (1.8%) with brighter N_2H^+ 3–2 integrated intensities than HCO^+ 3–2 lines. In contrast, the CHaMP survey (Census of High- and Medium-mass Protostars; Barnes 2010, Barnes et al. 2011) does not find any high-mass clumps in the their follow-up mapping survey of 303 sources in the fourth quadrant with N_2H^+ 1–0 integrated intensities larger than HCO^+ 1–0 intensities (see Figure 3 of Barnes et al. 2013). Mapping observations of HCO^+ 3–2 and N_2H^+ 3–2 toward IRDCs with BGPS clumps have revealed significant chemical differentiation of these two species on clump scales (see Battersby et al. 2010). Our survey indicates that, while rare, N_2H^+-brighter sources do occur.

Schlingman et al. (2011) explored the N_2H^+/HCO^+ 3–2 ratio toward the subset of 1882 sources observed and found a lack of correlation in the molecular intensity ratio and 1.1 mm flux density. The complete set of observations confirms this lack of correlation ($r_{corr} = 0.02$; Figure 10). We also observe a lack of correlation in the molecular ratio compared to the gas kinetic temperature measured using NH_3 observations ($r_{corr} = 0.01$;

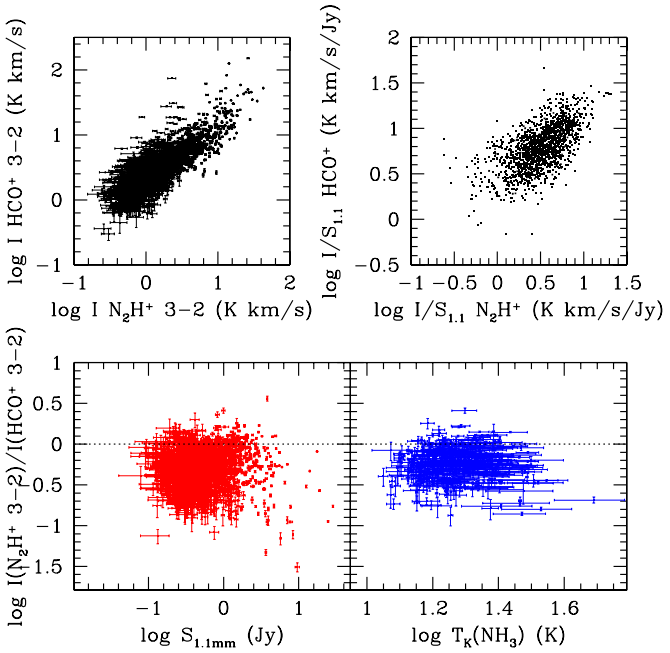

Figure 10. Top left: a strong correlation is observed between the HCO^+ and N_2H^+ 3–2 integrated intensities. Top right: a weaker correlation is observed between HCO^+ and N_2H^+ 3–2 integrated intensity to 1.1 mm flux density ratio. Errorbars have been suppressed to better display the points. Bottom left:the integrated intensity ratio N_2H^+ / HCO^+ 3–2 vs. 1.1 mm flux density from v2.0 maps. Bottom right: the integrated intensity ratio N_2H^+ / HCO^+ 3–2 vs. gas kinetic temperature determined from NH_3 observations.

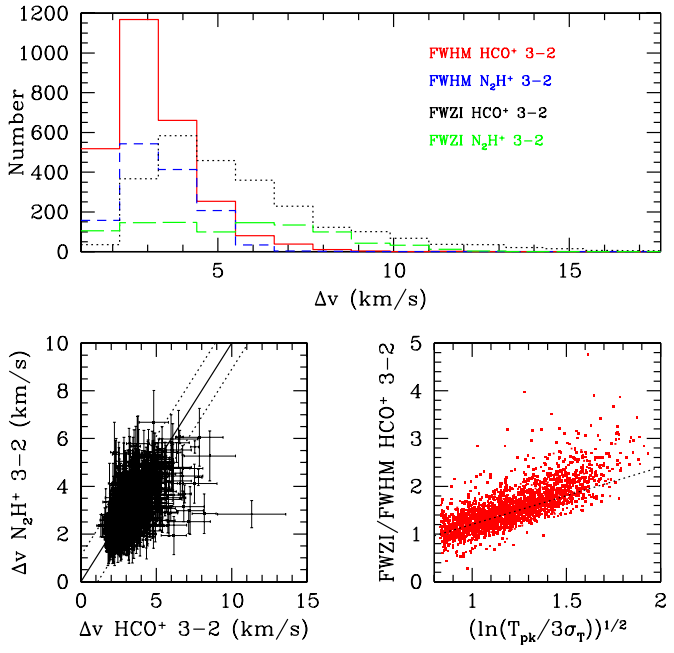

Figure 11. Top: histograms of HCO^+ 3–2 FWHM (solid red line), N_2H^+ 3–2 FWHM (short-dashed blue line), HCO^+ 3–2 FWZI (dotted black line), and N_2H^+ 3–2 FWZI (long-dashed green line). Bottom right: a correlation is observed between the N_2H^+ 3–2 and HCO^+ 3–2 line widths. A solid 1:1 line is plotted with dashed lines offset by the velocity resolution of one channel (1.1 km s^{-1}). Bottom right: the ratio of FWZI/FWHM for HCO^+ 3–2 correlates against $\sqrt{\ln(T_{\rm pk}/3\sigma_{T_{\rm mb}})}$. The dashed line shows the expected relationship for a Gaussian line shape.

Figure 10). At 30″ resolution, the 1.1 mm continuum, HHT, and GBT spectroscopic observations probe a spatial extent of 0.73 pc (D/5 kpc). This is very similar to the median size of BGPS clumps 0.75 pc found by Schlingman et al. BGPS clumps are very unlikely to be single massive cores (median $M \sim 300\ M_\odot$; Schlingman et al. 2011), but are likely to be composed of multiple smaller cores as confirmed by recent higher angular resolution observations (M. Merello et al., in preparation). The lack of a significant correlation in the molecular ratio with 1.1 mm flux suggests that there is variation in the fraction of cold, dense, CO-depleted gas between cores that are in BGPS clumps. This result can also be explained by the multiple core hypothesis if the cores within a BGPS clump have different average gas kinetic temperatures. This hypothesis may be tested with interferometric observations. The 113 sources with an intensity ratio of $N_2H^+/HCO^+ > 1$ are candidates for containing a dense, cold core within the clumps even though the beam-averaged gas kinetic temperature spans a factor of three.

4.3. Line Width and Full Width Zero Intensity

The distributions of FWHM line width, Δv, for HCO^+ and N_2H^+ 3–2 spectra with a flag = 1 that are well fit by a Gaussian line shape are shown in Figure 11. These distributions for the full catalog are similar to those found by Schlingman et al. (2011) with a median line width of 3.3 km s^{-1} for both HCO^+ 3–2 and for N_2H^+ 3–2. Both distributions are positively skewed, showing a small tail that reaches line widths up to 16 km s^{-1}. There are 559 HCO^+ 3–2 detections with measured $\Delta v < 2.2$ km s^{-1}; some of these 559 sources may have smaller Δv but we are limited by the velocity resolution (1.1 km s^{-1}) of the spectrometer. In comparison, Wienen et al. (2012) find that the observed line width of NH_3 (1,1) is ∼2 km s^{-1} with very few sources below 1 km s^{-1} (their spectral resolution is a factor of two better than this survey at 0.5 km s^{-1}). The HCO^+ and N_2H^+ line widths observed in this survey are plotted against each other in Figure 11. A few sources have HCO^+ 3–2 line widths that are larger than their corresponding N_2H^+ 3–2 line width, but most sources cluster around the 1:1 line.

The measured HCO^+ and N_2H^+ 3–2 line widths are compared to the observed 1.1 flux density and gas kinetic temperatures in Figure 12. None of these plots are well correlated; however, there are some discernible trends. HCO^+ 3–2 line width has a lower bound that increases with 1.1 mm flux density. For instance, sources with $S_{1.1} > 1$ Jy have Δv(HCO^+ 3–2) > 1.6 km s^{-1} while sources with $S_{1.1} > 10$ Jy have Δv(HCO^+ 3–2) > 5 km s^{-1}. Similarly, there is an increasing lower bound for line width with kinetic temperature. All Δv(HCO^+ 3–2) < 1.5 km s^{-1} have $T_k < 20$ K while all sources with $T_k > 23$ K have Δv(HCO^+ 3–2) > 3 km s^{-1}. The highest flux density and highest gas kinetic temperatures tend to have large (>few km s^{-1}) line widths.

The observed line widths are typically more than an order of magnitude larger than the expected thermal broadening in the line ($0.17\,{\rm km\,s^{-1}}\sqrt{T_k/18.3\,{\rm K}}$). If the non-thermal contribution to the line widths in the clumps is due to turbulent motions, then the observed values indicate that supersonic turbulence dominates BGPS clumps. Schlingman et al. (2011) showed that the standard supersonic turbulence scaling relationships for molecular clouds measured in CO (Larson's Law; Larson 1981) de-correlates in the dense gas tracers. This may be due to dissipation of turbulence in the denser molecular gas; however, the observed line widths are not systematically smaller than the predicted relationship for sizes below 1 pc from Larson's Law determined from CO clouds (see Schlingman et al. 2011). Alternatively, re-injection of turbulence by star formation likely

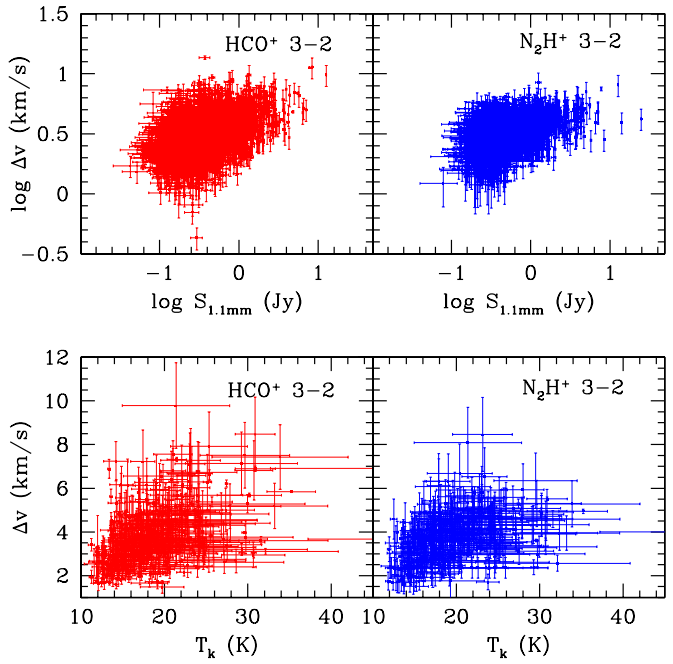

Figure 12. HCO^+ 3–2 FWHM (top left) and the N_2H^+ 3–2 FWHM (top right) vs. 1.1 mm flux density. The HCO^+ 3–2 FWHM (bottom left) and the N_2H^+ 3–2 (bottom right) vs. gas kinetic temperature.

(A color version of this figure is available in the online journal.)

occurs within a subset of the clumps (Murray 2011). Higher flux density sources and warmer sources are more likely to harbor embedded protostars (see Dunham et al. 2011b) whose winds and outflows may contribute to the turbulent gas motions within the BGPS clump.

Assigning the entire observed line width to turbulence is difficult though since unresolved bulk flows in the gas may also contribute to Δv. In nearby molecular clouds, velocity gradients of 1 km s^{-1} kpc^{-1} have been measured as well as inflowing motions along filaments (e.g., Kirk et al. 2013). Examples of bulk flows may be seen in the HCO^+ 3–2 spectra from this survey which display a self-absorbed blue asymmetry (see Section 4.5). Optical depth will also increase the line width. An optical depth of $\tau = 10$ will double the observed line width (Phillips et al. 1979; Shirley et al. 2003; see Section 4.4). The observed line width is likely a combination of unresolved bulk motions (gradients or flows), optical depth effects, and supersonic turbulence. Detailed study of the kinematics within BGPS clumps requires the higher spatial resolution currently only possible with interferometers.

We also find a lack of correlation between the N_2H^+ / HCO^+ molecular ratio and the observed line width. There are BGPS source with a molecular intensity ratio > 1 and with large > 5 km s^{-1} line widths. This chemical ratio does not depend on the amount of turbulence in the clump.

The full width zero intensity (FWZI) of a spectral line is the width of the line at the $3\sigma_{T_{\rm mb}}$ level. While the measured FWZI depends on the rms noise level in the spectrum, it can be determined for any line shape whereas the FWHM is determined from the fit of a Gaussian line shape. We calculate the FWZI for HCO^+ 3–2 spectra by finding the velocity of the first spectral channel on each side of the line peak which has a $T_{\rm mb} < 3\sigma_{T_{\rm mb}}$. The resulting HCO^+ FWZI are quantized by the channel spacing (1.1 km s^{-1}). For low signal-to-noise spectra, the quoted FWZI will be a lower limit to the true value. We only report FWZI for detections with $T_{\rm mb} \geqslant 6\sigma_{T_{\rm mb}}$ (2471 HCO^+ 3–2 detections).

The histogram of FWZI is plotted in Figure 11. The median FWZI for HCO^+ 3–2 lines is 4.5 km s^{-1}. The distribution has a tail of FWZI out to 32.5 km s^{-1}. The largest FWZI corresponds to source 6901 (G081.680+00.540), an outflow associated with the famous DR21 complex (see Davis & Smith 1996). There are 38 sources with FWZI > 15 km s^{-1}. These objects are strong outflow candidates.

For a Gaussian line shape, the FWZI is directly related to the peak signal-to-noise of the spectrum by

$$\frac{\rm FWZI}{\Delta v} = \frac{1}{\sqrt{2}}\sqrt{\ln(T_{\rm pk}/3\sigma_T)}, \quad (2)$$

where Δv is the FWHM. The ratio of FWZI/FWHM is plotted in Figure 11 for sources with a HCO^+ flag = 1 and shows a distinct correlation that generally follows the line predicted for a Gaussian line shape. The upward trend of FWZI/FWHM away from the dashed line in Figure 11 represent sources with non-Gaussian line shapes indicative of asymmetries or line wings in the spectra. However, most sources in the survey have line shapes that are consistent with a Gaussian line shape. We discuss self-absorbed profiles in detail in Section 4.5.

4.4. Optical Depth and Excitation Temperature

The optical depth in the HCO^+ 3–2 line may be determined from observations of an isotopologue and the radiative transfer equation assuming that the excitation temperature of the HCO^+ and $H^{13}CO^+$ 3–2 transitions are identical and that there is no fractionation between the interstellar ratio $[^{13}C]/[^{12}C]$ the molecular $[H^{13}CO^+]/[HCO^+]$ ratio. The peak optical depth of the HCO^+ 3–2 transition is determined from the nonlinear equation

$$\frac{T_{\rm mb}(HCO^+)}{T_{\rm mb}(H^{13}CO^+)} = \frac{1-\exp(-\tau)}{1-\exp(-\tau\frac{[^{13}C]}{[^{12}C]})}. \quad (3)$$

Observations were made during the final shift of observing in 2012 December in the $H^{13}CO^+$ 3–2 line (260.255339 GHz) toward 48 v1.0.1 sources in the Gem OB 1 star formation complex ($188^\circ < l < 193^\circ$; see Reipurth & Yan 2008) with HCO^+ 3–2 detections. Emission was detected for 34 sources (71%). Every source with a $H^{13}CO^+$ 3–2 detection has an optically thick HCO^+ 3–2 line with the average optical depth for this subset of $\tau = 10.2 \pm 4.7$ assuming $[^{13}C]/[^{12}C] = 50$ (see Table 4). Sources with $H^{13}CO^+$ 3–2 non-detections are generally weak in HCO^+ 3–2 resulting in an average 3σ upper limit of $\tau < 20$. It is likely that even these weak HCO^+ lines are optically thick.

Due to the large optical depth observed we can solve for the excitation temperature in the HCO^+ 3–2 line,

$$T_{\rm ex}^{\rm obs} = \frac{h\nu/k}{\ln\left(1+\frac{h\nu/k}{T_{\rm mb}/f+J_\nu(T_{\rm cmb})}\right)}, \quad (4)$$

where f is the filling fraction of emission and $J_\nu(T) = h\nu/k/(\exp(h\nu/kT)-1)$ is the Planck function in temperature units. The observed excitation temperatures are shown in Figure 13, assuming $f = 1$, plotted against the observed optical depth for sources associated with Gem OB 1. The average excitation temperature is $T_{\rm ex}^{\rm obs} = 5.3 \pm 2.0$ K, much lower than typical gas kinetic temperatures observed toward BGPS sources

Table 4
HCO^+ 3–2 Optical Depth from $H^{13}CO^+$ 3–2 Observations in Gemini

Number	Source	$T_{mb}(H^{13}CO^+)$ (K)	$\sigma_{T_{mb}}$ (K)	$\tau(HCO^+)$[a]	σ_τ
7460	G188.792+01.027	0.363	0.043	6.61	0.98
7461	G188.948+00.883	1.303	0.035	8.54	0.33
7462	G188.975+00.911	0.208	0.047	10.84	3.32
7463	G188.991+00.859	0.067	0.035	4.23	2.86
7464	G189.015+00.823	0.225	0.040	12.64	3.16
7465	G189.030+00.781	1.273	0.048	11.81	0.60
7471	G189.682+00.185	0.316	0.040	17.44	3.60
7472	G189.713+00.335	0.136	0.040	23.81	14.90
7473	G189.744+00.335	0.110	0.031	8.26	3.16
7474	G189.776+00.343	0.897	0.033	17.13	1.08
7475	G189.782+00.265	0.280	0.044	23.45	6.53
7476	G189.782+00.323	...	0.040	<6.74	...
7477	G189.783+00.433	...	0.036	<12.17	...
7478	G189.783+00.465	...	0.047	<34.5	...
7479	G189.788+00.281	0.102	0.019	9.45	2.75
7480	G189.789+00.291	0.082	0.042	7.03	4.43
7481	G189.804+00.355	0.259	0.038	10.09	1.93
7482	G189.810+00.369	0.137	0.041	6.55	2.43
7483	G189.831+00.343	0.138	0.021	7.73	1.61
7484	G189.834+00.317	0.147	0.041	8.96	3.17
7485	G189.836+00.303	...	0.033	<14.69	...
7486	G189.864+00.499	0.095	0.049	3.18	2.18
7487	G189.879+00.319	...	0.041	<24.86	...
7488	G189.885+00.319	0.090	0.017	12.71	4.55
7489	G189.888+00.303	0.118	0.035	11.26	4.56
7490	G189.921+00.331	...	0.041	<8.11	...
7491	G189.950+00.231	0.104	0.045	5.67	3.00
7492	G189.951+00.331	0.382	0.042	16.68	2.71
7493	G189.990+00.353	...	0.048	<50.30	...
7494	G190.006+00.361	0.140	0.041	22.16	11.79
7495	G190.044+00.543	...	0.045	<21.24	...
7497	G190.063+00.679	...	0.043	<37.16	...
7498	G190.171+00.733	0.289	0.042	15.45	3.56
7499	G190.192+00.719	0.087	0.040	13.12	9.33
7500	G190.240+00.911	0.076	0.023	7.67	3.22
7501	G192.581−00.043	0.790	0.042	9.22	0.64
7502	G192.596−00.051	0.260	0.042	4.34	0.86
7503	G192.602−00.143	...	0.045	<18.08	...
7505	G192.629−00.157	0.144	0.040	14.07	5.69
7506	G192.644+00.003	0.074	0.043	4.64	3.32
7507	G192.662−00.083	...	0.038	<20.80	...
7508	G192.719+00.043	...	0.048	<9.60	...
7509	G192.764+00.101	0.160	0.050	5.63	2.08
7510	G192.816+00.127	...	0.022	<5.73	...
7511	G192.968+00.093	...	0.051	<10.03	...
7512	G192.981+00.149	0.250	0.043	6.66	1.40
7513	G192.985+00.177	0.145	0.052	5.72	2.43
7514	G193.006+00.115	0.268	0.050	8.66	2.00

Note. [a]Upper limits correspond to $3\sigma_{T_{mb}}$ upper limits for $H^{13}CO^+$ 3–2.

with NH_3 T_k determinations (Figure 5). Assuming that HCO^+ emission is optically thick for all BGPS sources, we can compare the excitation temperature with T_k for this subsample. The average $T_{ex}^{obs} = 5.5 \pm 1.4$ K is very similar to the average found for sources in Gem OB 1. The observed excitation temperatures are weakly correlated with the gas kinetic temperature (Figure 14) with sources that have $T_{ex}^{obs} > 8$ K typically having $T_k > 20$ K.

We compare the observed T_{ex}^{obs} to the excitation of the 3–2 transition from a single zone radiative transfer model. The top right panel of Figure 13 shows the model excitation temperature

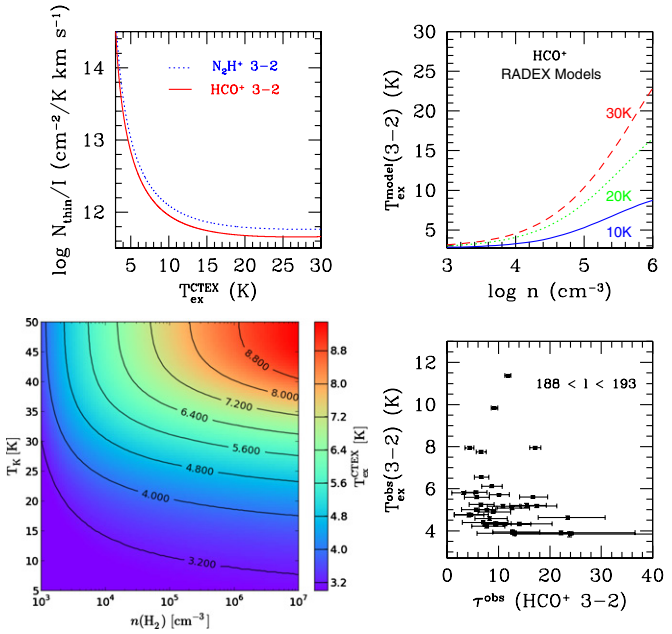

Figure 13. Top left: optically thin column density of HCO^+ 3–2 (solid red line) and N_2H^+ 3–2 (dotted blue line) vs. T_{ex}^{CTEX}. Below $T_{ex}^{CTEX} = 10$ K, the column density becomes a sensitive function of excitation temperature. Top right: the model excitation temperature of HCO^+ 3–2 vs. volume density for constant density, constant kinetic temperature radiative transfer models with $\log N/\Delta v = 13.5$ (RADEX; van der Tak et al. 2007). The blue (solid) curves is $T_k = 10$ K, the green (dotted) curve is $T_k = 20$ K, and the red (dashed) curve is $T_k = 30$ K. Bottom left: contours of T_{ex}^{CTEX} for HCO^+ 3–2 observations from constant density, constant kinetic temperature models. Bottom right: peak optical depth of the HCO^+ 3–2 line calculated from $H^{13}CO^+$ 3–2 observations. HCO^+ 3–2 emission is typically optically thick and sub-thermally populated in the physical conditions found in BGPS clumps.

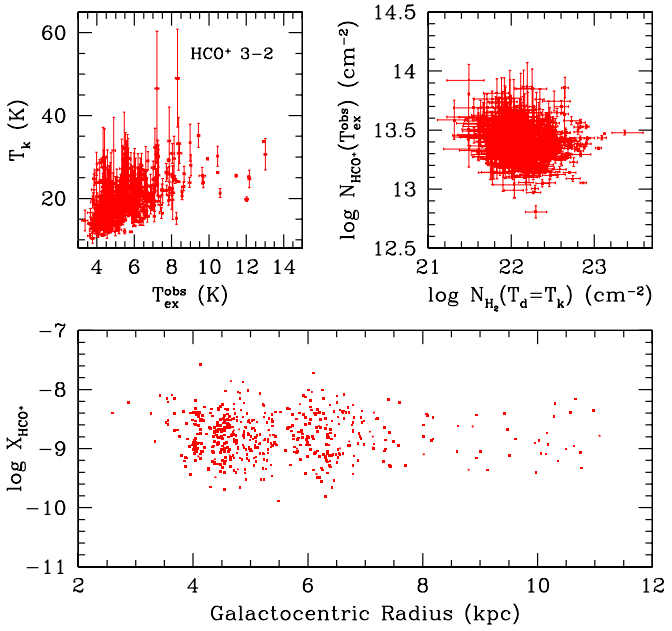

Figure 14. Top left: the gas kinetic temperature vs. the excitation temperature determined from the HCO^+ 3–2 line. Top right: the column density of HCO^+ vs. the H_2 column density assuming $T_d = T_k$. Only the subset of sources with NH_3 observations are plotted. Bottom: The HCO^+ 3–2 abundance does not vary systematically with Galactocentric radius.

for single density, single kinetic temperature models calculated using *RADEX* (van der Tak et al. 2007). The three curves

correspond to gas kinetic temperatures spanning the range of $T_k = 10$ to 30 K. For the typical average volume densities probed toward BGPS clumps of 10^3–$10^{4.5}$ cm^{-3} (Schlingman et al. 2011; Dunham et al. 2011), the model excitation temperature is < 7 K with $T_{\rm ex}^{\rm model} \ll T_k$. $T_{\rm ex}^{\rm model}$ agrees well with the observed median $T_{\rm ex}^{\rm obs}$ indicating that most of the 3122 HCO$^+$ 3–2 lines observed in this survey are very sub-thermally populated. Unfortunately, it would a prohibitively long survey to determine the optical depth in all 3122 HCO$^+$ 3–2 detections using H^{13}CO$^+$ 3–2 observations.

The excitation temperature must be determined or assumed to derive a column density from the observed integrated intensity. In the optically thin, constant excitation temperature limit ($T_{\rm ex} = T_{\rm ex}^{\rm CTEX}\ \forall J$), the total column density derived from the integrated intensity of HCO$^+$ and N$_2$H$^+$ 3–2 emission is given by

$$N_{\rm thin} = \frac{8\pi k \nu^2 f}{7hc^3 A_{3-2}} \frac{Q(T_{\rm ex}) J_\nu(T_{\rm ex}) e^{E_u/kT_{\rm ex}}}{J_\nu(T_{\rm ex}) - J_\nu(T_{\rm cmb})} \int T_{\rm mb}\, dv, \qquad (5)$$

where A_{3-2} is the Einstein spontaneous emission coefficient (1.476×10^{-3} s^{-1} for HCO$^+$ 3–2 and 1.259×10^{-3} s^{-1} for N$_2$H$^+$ 3–2), Q is the partition function and E_u/k is the energy of the upper ($J = 3$) level (25.68 K for HCO$^+$ 3–2 and 26.83 K for N$_2$H$^+$ 3–2). For the 3–2 transitions of both molecules, the column density becomes a sensitive function of $T_{\rm ex}$ below 10 K (Figure 13). The excitation temperature derived from Equation (3) ($T_{\rm ex}^{\rm obs}$) applies only for the $J = 3$ level, but the excitation temperature for the CTEX approximation is potentially different because of non-LTE excitation. The bottom left panel of Figure 13 calculates $T_{\rm ex}^{\rm CTEX}$ from Equation (4) for a grid of models with constant density and constant kinetic temperature assuming a total HCO$^+$ column density of 3.16×10^{13} cm^{-2} ($\log N = 13.5$ which is the standard assumption used to calculate $n_{\rm eff}$). The plotted contours span $3.1 < T_{\rm ex}^{\rm CTEX} < 7$ K for the range of average kinetic temperature measured from NH$_3$ observations. This range overlaps the $\langle T_{\rm ex}^{\rm obs} \rangle$ calculated from Equation (3) indicating that assuming $T_{\rm ex}^{\rm obs} \approx T_{\rm ex}^{\rm CTEX}$ in Equation (4) is a reasonable approximation for BGPS clumps. Using this approximation, the median HCO$^+$ column density is 2.5×10^{13} cm^{-2}.

If we assume 5 K as a typical excitation temperature and assume the filling fraction of emission is $f \approx 1$, the HCO$^+$ 3–2 integrated intensities may be converted to optically thin column densities using the scale factor $N_{\rm HCO^+}/I_{\rm HCO^+} = 6.9 \times 10^{12}$ cm^{-2} K^{-1} (km s^{-1})$^{-1}$ and the N$_2$H$^+$ 3–2 emission scale factor of $N_{\rm N_2H^+}/I_{\rm N2H^+} = 1.0 \times 10^{13}$ cm^{-2} K^{-1} (km s^{-1})$^{-1}$. The corresponding 3σ upper limit to the optically thin HCO$^+$ 3–2 column density in this survey is $N_{3\sigma} > 1.2 \times 10^{12}$ cm^{-2}. However, we know that the HCO$^+$ 3–2 line is likely optically thick from the results of H^{13}CO$^+$ 3–2 observations; therefore, we should apply a correction to the optical depth of $N = N_{\rm thin}\tau/(1-e^{\tau})$ (Goldsmith & Langer 1999). The HCO$^+$ column densities shown in Figure 14 are likely lower limits because we do not know the true optical depth for sources outside Gem OB 1.

We plot the HCO$^+$ column density versus the total H$_2$ column density calculated from the 1.1 mm peak flux density assuming Ossenkopf & Henning (OH5) opacities and that the dust temperature is equal to the gas kinetic temperature from NH$_3$ observations (Figure 14). Gas kinetic temperature and dust temperature are only expected to be well coupled at high densities ($n > 10^5$ cm^{-3}; see Goldsmith 2000); however, in the absence of other information, it is a better approximation than assuming all sources are at the same dust temperature. The plotted column density errorbars are purely statistical errors based on the uncertainty in $\sigma_{T_{\rm mb}}$. The total uncertainty in the HCO$^+$ column density is dominated by the uncertainty in the unknown filling fraction of emission and the uncertainty in the unknown optical depth which would likely increase the column density by factors of a few. With these caveats in mind, we plot the HCO$^+$ column density and abundances in Figure 14. In contrast with the integrated intensity correlation (Section 4.2), there is no correlation between the HCO$^+$ and H$_2$ column densities. This result again highlights the importance of the excitation conditions and not the total molecular column density in driving the observed intensity correlations. A similar lack of correlation was also observed for NH$_3$ column densities versus H$_2$ column densities by Wienen et al. (2012). We find a median HCO$^+$ abundance of 1.6×10^{-9}. The HCO$^+$ abundance also shows no discernible trend with Galactocentric radius (Figure 14). This result is in contrast with NH$_3$ observations which show a decrease by a factor of seven in abundance with Galactocentric radius (Dunham et al. 2011a). Both studies are limited by a paucity of sources at large Galactocentric radius with measured gas kinetic temperatures.

Unfortunately, we cannot easily calculate the optical depth in the N$_2$H$^+$ 3–2 line because the 45 hyperfine lines are too heavily blended to obtain believable constraints. Furthermore, observations of the ^{15}NNH$^+$ isotopologue is prohibitive because the interstellar [^{15}N]/[^{14}N] abundance is a factor of 5–10 smaller than the ISM [^{13}C]/[^{12}C] abundance (Wilson & Rood 1994; Adande & Ziurys 2012). N$_2$H$^+$ 3–2 is also very likely sub-thermally populated based on our radiative transfer calculations. Given the more than order of magnitude uncertainties, we do not report column densities for N$_2$H$^+$ 3–2 emission. We recommend observations of the N$_2$H$^+$ 1–0 line where the hyperfine splitting is more easily resolved (e.g., Pirogov et al. 2003; Pirogov et al. 2007; Reiter et al. 2011a; Barnes et al. 2013).

4.5. Self-absorbed Line Profiles

While most HCO$^+$ 3–2 lines in the survey are believed to have $\tau > 1$ based on limited H^{13}CO$^+$ 3–2 observations and comparison to radiative transfer models (Section 4.4), there is a small percentage of sources that display clear line asymmetries indicative of kinematic motions coupled with very optically thick lines. For a HCO$^+$ 3–2 line profile to be classified as self-absorbed, the profile must show two peaks and an absorption dip over the span of at least three channels (3.3 km s^{-1}) with the N$_2$H$^+$ 3–2 line profile having a single-peak (HCO$^+$ flag = 3 while N$_2$H$^+$ flag = 1). This situation occurs for 80 (1.3%) sources (Table 5). Self-absorbed line profiles are extremely rare in this survey. This may, in part, be due to the low spectral resolution (1.1 km s^{-1}) required to cover the full velocity range (-60 to 170 km s^{-1}) of sources in the longitude range observed in the first quadrant.

We may classify the self-absorbed sources as blue, red, or equal asymmetries by the location of the $v_{\rm lsr}$ maximum. 47 sources have a clear blue asymmetry while 26 sources have a clear red asymmetry and 7 sources have equal height peaks. The blue excess for the subset of sources showing distinct self-absorption is $(N_B - N_R)/N_{\rm SA} = 0.57$. These 80 sources (listed in Table 5) are excellent high-mass, large-scale collapse candidates (see Reiter et al. 2011b) and should be followed up at higher spatial resolution.

Table 5
HCO^+ 3–2 Line Asymmetries

Number	Source	Catalog[a]	HCO^+ Flag	N_2H^+ Flag	Asymmetry[b]
1363	G008.458−00.224	2	3	1	b
1377	G008.670−00.356	2	3	1	b
1398	G008.872−00.318	2	3	1	r
1412	G009.212−00.202	2	3	1	b
1421	G009.620+00.194	2	3	1	r
1466	G010.214−00.324	1	3	3	b
1491	G010.416−00.030	2	3	0	b
1518	G010.681−00.028	1	3	1	b
1521	G010.693−00.404	1	3	0	b
1584	G011.083−00.536	1	3	1	b
1659	G011.947−00.036	1	3	1	r
1780	G012.809−00.200	1	3	1	r
1796	G012.861−00.272	1	3	1	r
1803	G012.889+00.490	1	3	1	b
1833	G012.999−00.358	1	3	1	r
1869	G013.211−00.142	1	3	1	r
1943	G013.816+00.003	2	3	0	b
1956	G013.882−00.143	2	3	1	b
2019	G014.244−00.071	1	3	1	e

Notes.
[a]Catalog number 1 = Schlingman et al. (2011) and 2 = new observations presented in this paper.
[b]b = blue-asymmetry, r = red asymmetric, e = equal asymmetry.
(This table is available in its entirety in a machine-readable form in the online journal. A portion is shown here for guidance regarding its form and content.)

5. CONCLUSIONS

In this paper, we have presented a complete spectroscopic catalog for all sources in the BGPS v1.0.1 source catalog with $7.^\circ5 \leqslant l \leqslant 194^\circ$ and characterized the properties of the molecular emission. Three thousand and twenty-six sources (50.5%) were detected with unique $v_{\rm LSR}$. HCO^+ 3–2 is a significantly better kinematic tracer of BGPS clumps than CO isotopologues with contamination from multiple velocity components rare (only 1.3%). The detection fraction of BGPS v1.0.1 sources is $>$ 50% for 1.1 mm sources with flux densities $>$ 200 mJy and $>$ 90% for flux densities $>$ 500 mJy. The majority of BGPS clumps appear to be physically associated with other clumps. This is the largest targeted dense gas survey of the Milky Way to date and traces the major spiral arm structures of the Milky Way in Galactocentric radius.

HCO^+ and N_2H^+ molecular intensities are well correlated with 1.1 mm flux density and with each other while molecular column densities are not well correlated with the total H_2 column density. HCO^+ 3–2 intensity is also correlated with gas kinetic temperature. HCO^+ 3–2 emission is likely optically thick and sub-thermally populated ($T_{\rm ex} \sim 5\,{\rm K} \ll T_k$) toward most BPGS clumps. These observed intensity correlations are most likely due to the sensitivity of the 3–2 transitions to excitation conditions probed by the dense gas. The molecular intensity ratio does not correlate with 1.1 mm flux density, T_k, or Δv. BGPS clumps are likely composed of smaller cores which may have a range of different chemical and excitation conditions. Sources with large N_2H^+/HCO^+ intensity ratios probably contain significant reservoirs of cold, dense gas. The median $\Delta v = 3.3$ km s^{-1} (FWHM) and is consistent with supersonic turbulence although optical depth and bulk motions within the core are contributors to the line width. The observed line width does not correlate with 1.1 mm flux density or T_k although the lower bound of Δv does correlated with both quantities.

In the coming months, source catalogs from the ATLASGAL and Hi-Gal continuum surveys of the Galaxy will be released. The kinematic data provided in this paper provides the necessary information for calculating kinematic distances. Future work by the BGPS team will use this spectroscopic catalog and expand the priors to better constrain Distance Probability Density Functions and statistically analyze the physical properties of BGPS clumps in different evolutionary stages and in different Galactic environments.

We sincerely thank the staff of the Arizona Radio Observatory—in particular, the operators Bob Moulton, John Downey, Patrick Fimbres, and Craig Sinclair—for their help and hospitality during observing. We also sincerely thank the referee for comments that improved the manuscript. This work was supported by NSF grant AST-1008577.

REFERENCES

Adande, G. R., & Ziurys, L. M. 2012, ApJ, 744, 194
Aguirre, J. E., Ginsburg, A. G., Dunham, M. K., et al. 2011, ApJS, 192, 4
Arzoumanian, D., André, P., Didelon, P., et al. 2011, A&A, 529, L6
Barnes, P. 2010, From Stars to Galaxies: Connecting our Understanding of Star and Galaxy Formation (http://conference.astro.ufl.edu/STARSTOGALAXIES, id.92)
Barnes, P. J., Ryder, S. D., O'Dougherty, S. N., et al. 2013, MNRAS, 432, 2231
Barnes, P. J., Yonekura, Y., Fukui, Y., et al. 2011, ApJS, 196, 12
Battersby, C., Bally, J., Jackson, J. M., et al. 2010, ApJ, 721, 222
Beuther, H., Tackenberg, J., Linz, H., et al. 2012, ApJ, 747, 43
Contreras, Y., Schuller, F., Urquhart, J. S., et al. 2013, A&A, 549, A45
Dame, T. M., Hartmann, D., & Thaddeus, P. 2001, ApJ, 547, 792
Dame, T. M., & Thaddeus, P. 2011, ApJL, 734, L24
Davis, C. J., & Smith, M. D. 1996, A&A, 310, 961
Dunham, M. K., Robitaille, T. P., Evans, N. J., II, et al. 2011a, ApJ, 731, 90
Dunham, M. K., Rosolowsky, E., Evans, N. J., II, Cyganowski, C., & Urquhart, J. S. 2011b, ApJ, 741, 110
Eden, D. J., Moore, T. J. T., Morgan, L. K., Thompson, M. A., & Urquhart, J. S. 2013, MNRAS, 431, 1587
Eden, D. J., Moore, T. J. T., Plume, R., & Morgan, L. K. 2012, MNRAS, 422, 3175
Elia, D., Molinari, S., Fukui, Y., et al. 2013, ApJ, 772, 45
Ellsworth-Bowers, T. P., Glenn, J., Rosolowsky, E., et al. 2013, ApJ, 770, 39
Encrenaz, T., & Moreno, R. 2002, in AIP Conf. Proc. 616, Experimental Cosmology at Millimetre Wavelengths, ed. M. De Petri & M. Gervasi (Melville, NY: AIP), 330
Evans, N. J., II. 1999, ARA&A, 37, 311
Foster, J. B., Jackson, J. M., Barnes, P. J., et al. 2011, ApJS, 197, 25
Foster, J. B., Rathborne, J. M., Sanhueza, P., et al. 2013, PASA, 30, 38
Ginsburg, A., Glenn, J., Rosolowsky, E., et al. 2013, APJS, 208, 14
Goldsmith, P. F., & Langer, W. D. 1999, ApJ, 517, 209
Hennebelle, P., & Falgarone, E. 2012, A&ARv, 20, 55
Ho, P. T. P., & Townes, C. H. 1983, ARA&A, 21, 239
Jackson, J. M., Rathborne, J. M., Shah, R. Y., et al. 2006, ApJS, 163, 145
Jørgensen, J. K., Schöier, F. L., & van Dishoeck, E. F. 2004, A&A, 416, 603
Kirk, H., Myers, P. C., Bourke, T. L., et al. 2013, ApJ, 766, 115
Larson, R. B. 1981, MNRAS, 194, 809
Men'shchikov, A., André, P., Didelon, P., et al. 2010, A&A, 518, L103
Molinari, S., Swinyard, B., Bally, J., et al. 2010a, PASP, 122, 314
Molinari, S., Swinyard, B., Bally, J., et al. 2010b, A&A, 518, L100
Murray, N. 2011, ApJ, 729, 133
Ossenkopf, V., & Henning, T. 1994, A&A, 291, 943
Palmeirim, P., André, P., Kirk, J., et al. 2013, A&A, 550, A38
Penzias, A. A., & Burrus, C. A. 1973, ARA&A, 11, 51
Phillips, T. G., Huggins, P. J., Wannier, P. G., & Scoville, N. Z. 1979, ApJ, 231, 720
Pirogov, L., Zinchenko, I., Caselli, P., & Johansson, L. E. B. 2007, A&A, 461, 523
Pirogov, L., Zinchenko, I., Caselli, P., Johansson, L. E. B., & Myers, P. C. 2003, A&A, 405, 639
Reid, M. J., Menten, K. M., Zheng, X. W., et al. 2009, ApJ, 700, 137

Reipurth, B., & Schneider, N. 2008, Handbook of Star Forming Regions, Vol. I, The Northern Sky ASP Monograph Publications, ed. B. Reipurth, 36
Reipurth, B., & Yan, C.-H. 2008, Handbook of Star Forming Regions, Vol. I, The Northern Sky ASP Monograph Publications, ed. B. Reipurth, 869
Reiter, M., Shirley, Y. L., Wu, J., et al. 2011a, ApJS, 195, 1
Reiter, M., Shirley, Y. L., Wu, J., et al. 2011b, ApJ, 740, 40
Robitaille, T. P., Churchwell, E., Benjamin, R. A., et al. 2012, A&A, 545, A39
Roman-Duval, J., Jackson, J. M., Heyer, M., et al. 2009, ApJ, 699, 1153
Rosolowsky, E., Dunham, M. K., Ginsburg, A., et al. 2010, ApJS, 188, 123
Salpeter, E. E. 1955, ApJ, 121, 161
Scalo, J. M. 1986, FCPh, 11, 1
Schlingman, W. M., Shirley, Y. L., Schenk, D. E., et al. 2011, ApJS, 195, 14
Shirley, Y. L., Evans, N. J., II, Young, K. E., Knez, C., & Jaffe, D. T. 2003, ApJS, 149, 375
Solomon, P. M., Rivolo, A. R., Barrett, J., & Yahil, A. 1987, ApJ, 319, 730
van der Tak, F. F. S., Black, J. H., Schöier, F. L., Jansen, D. J., & van Dishoeck, E. F. 2007, A&A, 468, 627
Weiland, J. L., Odegard, N., Hill, R. S., et al. 2011, ApJS, 192, 19
Wienen, M., Wyrowski, F., Schuller, F., et al. 2012, A&A, 544, A146
Wilson, T. L., & Rood, R. 1994, ARA&A, 32, 191
Wolfire, M. G., McKee, C. F., Hollenbach, D., & Tielens, A. G. G. M. 2003, ApJ, 587, 278
Wynn-Williams, C. G., Becklin, E. E., & Neugebauer, G. 1974, ApJ, 187, 473